

# Postbuckling optimisation of a variable angle tow composite wingbox using a multi-modal Koiter approach

Francesco S. Liguori<sup>a,\*</sup>, Giovanni Zucco<sup>b</sup>, Antonio Madeo<sup>a</sup>, Domenico Magisano<sup>a</sup>, Leonardo Leonetti<sup>a</sup>,  
Giovanni Garcea<sup>a</sup>, Paul M. Weaver<sup>b</sup>

<sup>a</sup>*Dipartimento di Ingegneria Informatica, Modellistica, Elettronica e Sistemistica, Università della Calabria, 87030 Rende (Cosenza), Italy*

<sup>b</sup>*School of Engineering and Bernal Institute, University of Limerick, Ireland*

---

## Abstract

The stiffness-tailoring capability of Variable Angle Tow (VAT) laminates gives enhanced freedom to design thin-walled structures. One key advantage of tow steering is the ability to redistribute stresses improving buckling performance, leading to reduction in material weight and costs. The aim of this work is to optimise the initial postbuckling behaviour of a recently proposed VAT composite wingbox. The optimisation process is based on a fibre path parameterisation. It involves seeking the stacking sequence that minimises the displacements occurring in the postbuckling regime. This problem is solved by coupling the multi-modal Koiter asymptotic approach implemented with a solid-shell Finite Element environment through stochastic optimisation strategies. Results obtained regarding different optimisation scenarios show a much improved performance for the buckling and postbuckling response of the wingbox with respect to the initial VAT design. Additionally, manufacturing constraints are readily included in the optimisation program. The possibility of performing an efficient and robust optimisation process of a complex structure with a multi-modal Koiter asymptotic approach is demonstrated, showing its viability as a design tool for buckling dominated structures. A parametric study regarding the influence of steering radii shows that overcoming the current manufacturing constraint on minimum radius is worthy of investigation.

*Keywords:* Wingbox, variable angle tow laminates, postbuckling optimisation, Koiter method, finite element method

---

## 1. Introduction

The increasing need for fuel-efficient aircraft places great emphasis on light weight structures. Inevitably, such drivers lead to thin-walled wing structures bringing buckling and postbuckling phenomena into consideration. Today, composite materials play a key role in many applications of large commercial aircraft due to their high specific structural properties [1]. Many aircraft, such as the Boeing 787 and the Airbus A350, have more than 50% by weight of composite materials.

The wingbox is the most important structural component of the wings and, in general, is the most complex and heavily loaded primary structure of an aircraft. Recently, Oliveri et al. [2] showed how the design possibilities of a composite wingbox can be increased further by using Variable Angle Tow (VAT) laminates. In VAT structures the fibre tows within a single layer are not restricted to straight trajectories, but can describe curvilinear paths. One of the first works to introduce this concept was by Cooper in 1972

---

\*Corresponding author

*Email addresses:* francesco.liguori@unical.it (Francesco S. Liguori), giovanni.zucco@ul.ie (Giovanni Zucco), antonio.madeo81@unical.it (Antonio Madeo), domenico.magisano@unical.it (Domenico Magisano), leonardo.leonetti@unical.it (Leonardo Leonetti), giovanni.garcea@unical.it (Giovanni Garcea), paul.weaver@ul.ie (Paul M. Weaver)

[3]. Afterwards, many scientists have shown that tailoring the in-plane stiffness over the plate platform allows pre-buckling stresses to be redistributed to supported regions, thereby increasing the critical buckling load considerably [4–10]. Less well known is that postbuckling behaviour can be improved by using VAT technology. In this regard, White and Weaver showed [11] that the well-known imperfection sensitivity of a cylindrical thin structure under compression loading can be eliminated by tailoring the fibre paths across the surface of cylindrical shells. Hence, stable plate-like postbuckling responses in cylindrical shells were documented for the first time.

VAT composite laminates manufactured via tow steering can increase the buckling capacity of composite structures, leading to reduced material weight and costs. In this sense, many previous works consider optimisation problems of the first linear buckling load [7, 12–14]. However, in this way it is not possible to take into account the interaction of buckling modes, which can lead to inaccurate evaluation of the structural behaviour. The most notable evidence of such response is the case of unstable post-critical behaviour and high imperfection sensitivity, as documented in [15–20]. In such cases, the collapse load can be noticeably overestimated.

For this reason, a more reliable description, which takes account of the full geometrically nonlinear behaviour, has also been investigated [21–23]. When dealing with this problem, use is often made of algorithms based on path following strategies [24, 25]. It can be stated that today they represent the standard technique to obtain the equilibrium path of thin-walled structures. However, there are situations in which the equilibrium path has to be evaluated many times, e.g. in optimisation processes and imperfection sensitivity analyses. In such cases, the suitability of path following methods breaks down, because the single run is overly time consuming with current computational capability. Consequently, the need for computational efficiency has guided research towards tools capable of furnishing information on the postbuckling behaviour with a reasonable computational cost. In this context the works based on semi-analytical solutions [26], generalised path-following approaches [27] and strategies based on Koiter’s theory of elastic stability [28] can be framed. With regard to this last topic, many works have been completed in recent years. Formulations based on a simplified structural model and a single buckling mode are employed in optimisation problems [11, 29], while imperfection sensitivity analyses are carried out in [30–33]. The Finite Element (FE) implementation of Koiter’s algorithm proposed by Casciaro [34] is an interesting strategy to analyse light weight structures. It is a relatively efficient alternative method to path following for capturing the initial postbuckling response [35–40]. The method is based on the projection of the equilibrium equations in the subspace of the buckling modes associated with the lowest critical loads. The important consequence of this description is the reduction of the size of the nonlinear system of equilibrium equations, thereby making its solution rapid and inexpensive. In fact, the number of equations of this Reduced Order Model (ROM) becomes of the order of tens, which corresponds to the number of buckling modes used in the asymptotic expansion.

Growing demand for slender and thinner aeronautical components leads to necessary consideration of nonlinear effects such as postbuckling behaviour [23]. However, the optimal stiffness distribution for maximising linear buckling load could contrast with that for maximising post-buckling performance [41]. Therefore, for these structures, it is necessary to improve both the buckling and postbuckling performances for a better structural response, as established by Raju et al. [23]. Recently, Liguori et al. [42] used a multi-modal Koiter algorithm for optimising the postbuckling behaviour of composite structures. This algorithm was coupled with a simple Monte Carlo Algorithm (MCA) to identify the stacking sequence that maximises collapse load. Stochastic strategies require many evaluations of the objective function to give a good estimate of the optimum solution, but the single run was cost-effective thanks to the efficiency of Koiter’s analysis in providing the nonlinear response. As such, the postbuckling optimisation strategy proved to be fast and robust.

Driven by these premises, the FE based multi-modal Koiter algorithm is used for the first time to optimise a primary VAT aeronautical structure, i.e. the wingbox proposed by Oliveri et al. [2]. As this structure has already been designed for maximising the linear buckling load, we decided to optimise the postbuckling response. Raju et al. [23] suggest the post-buckling behaviour can be optimised by the minimisation of the end-shortening strain or the maximum postbuckling out-of-plane-displacement for a given compressive load. In our case, in order to avoid reduction of aerodynamic and aeroelastic performance, we chose to minimise the

out-of-plane-displacement occurring in the postbuckling regime, which can affect the aerodynamic efficiency of the wing shape [43]. The strategy previously proposed [42] is extended to address the requirements of the optimisation of a full scale structure.

Constraints on the maximum displacement (i.e. a fixed percentage of the wingspan) and on the maximum principal strain (i.e.  $2500\mu\epsilon$  as used in [2] in the design process) are readily considered during the optimisation procedure. Then, using the results of Clancy et al. [44], the manufacturability of the solution is ensured by including constraints on the steering radii of the fibre paths. Stochastic strategies are widely employed techniques to find global solutions for non-convex nonlinear optimisation problems. An improved version of MCA, based on an iteratively repeated zooming analysis, is here used to obtain a good estimate of the optimal solution. In addition, a Genetic Algorithm (GA) that represents a robust and commonly-used stochastic algorithm is used to validate results. The significant number of objective function evaluations required by both approaches is made possible by using Koiter’s analysis, which for the first time is employed in a framework that includes manufacturing constraints. Moreover, during the optimisation process, this method allows the effects of geometrical imperfections to be considered. Accounting for the imperfection sensitivity in the design is crucial in many cases to avoid naive optimisation [45]. The ”worst” imperfection shape in the subspace of those evaluated as a linear combination of buckling modes is detected with a successful procedure that has been previously used [31, 42]. This represents a reasonable description of a worst-case imperfection to assess the imperfection sensitivity in practical problems [30]. More general shapes could, however, be considered as in the work by Deml and Wunderlich [46]. Finally, a parametric study regarding the influence of the steering radii is conducted. It shows how the constraint on the steering radius has a significant effect on the optimal solution.

The starting point of this work is the description of the multi-modal Koiter method in the FE environment using a mixed solid-shell finite element obtained from the Hellinger-Reissner variational principle. The solid-shell formulation is briefly recalled and extended to variable stiffness laminates in Section 2. The fundamental equations of Koiter’s asymptotic method are presented in Section 3. Section 4 considers the description of the wingbox and its optimisation. In Section 5 the reference wingbox is analysed with Koiter’s method and the results of the optimisation are presented and discussed. Finally, conclusions are drawn in Section 6.

## 2. The hybrid solid-shell finite element for variable stiffness structures

The First Order Shear Deformation Theory solid-shell FE proposed previously [47, 48] is hereby extended to variable stiffness laminates. It is directly derived from the 3D continuum of Cauchy and uses the Green strain measure. The starting functional is the Hellinger-Reissner variational principle, which considers both displacements and stresses as primary variables. Consequently, the strain energy has only a cubic polynomial dependence on the configuration variables. The element has eight nodes, each of them with translational degrees of freedom only. The stress field interpolation employs 18 parameters. With 24 displacement degrees of freedom, the FE has the same number of variables as a four-noded shell with drilling rotations [49]. Many advantages of using a Hellinger-Reissner based FE for describing geometrically nonlinear problems have been discussed in the literature [40, 49]. Among them, an important benefit resides in the fact that the stresses are directly extrapolated when performing Koiter’s analysis. This process avoids locking phenomena that affect the accuracy of the ROM when stresses are derived from extrapolated displacements, as happens in displacement-based formulations. In addition, the use of the hybrid stress solid-shell FE improves the accuracy and range of validity of the asymptotic expansion [38, 48].

### 2.1. Formulation

We denote the mixed strain energy associated with the Hellinger-Reissner variational principle as  $\Phi[u]$ . This scalar quantity can be expressed, as is usual in the FE context, as the sum of element contributions

$$\Phi[u] = \sum_e \Phi_e[u] \quad (1)$$

where  $\Phi_e[u]$  is given by

$$\Phi_e[u] = \int_{\Omega_e} \left( \mathbf{t}^T \boldsymbol{\rho}[\mathbf{d}] - \frac{1}{2} \mathbf{t}^T \mathbf{C}_\rho^{-1} \mathbf{t} \right) d\Omega_e \quad (2)$$

and where  $\boldsymbol{\rho}[\mathbf{d}]$  and  $\mathbf{t}$  are the vectors collecting the generalised strains and stresses components for the given structural model,  $\Omega_e$  is the finite element domain and  $\mathbf{d}$  is the displacement field. All quantities are functions of a suitable abscissa coordinate  $\zeta$  which defines the mid-plane of the shell.

Generalised stresses and displacements are interpolated, on the element, in terms of the kinematics  $\mathbf{d}_e$  and the static  $\boldsymbol{\beta}_e$  finite element variables

$$\mathbf{d}[\zeta] = \mathbf{N}_u[\zeta] \mathbf{d}_e \quad \mathbf{t}[\zeta] = \mathbf{N}_\sigma[\zeta] \boldsymbol{\beta}_e \quad (3)$$

which, when substituted in Eq.(2), lead to the discrete form of the strain energy

$$\Phi_e[u] = \boldsymbol{\beta}_e^T \boldsymbol{\rho}_e[\mathbf{d}_e] - \frac{1}{2} \boldsymbol{\beta}_e^T \mathbf{H}_e \boldsymbol{\beta}_e \quad (4)$$

where

$$\mathbf{H}_e = \int_{\Omega} \mathbf{N}_\sigma^T \mathbf{C}_\rho^{-1} \mathbf{N}_\sigma d\Omega_e, \quad \boldsymbol{\rho}_e[\mathbf{d}_e] = \int_{\Omega} \mathbf{N}_\sigma^T \boldsymbol{\rho}[\zeta, \mathbf{N}_u[\zeta] \mathbf{d}_e] d\Omega_e \quad (5)$$

A typical limitation of FE analysis of VAT structures is that the fibre angle distribution is treated as piecewise constant within each element. In this way, it is easy to introduce spurious stress and strain residuals (i.e. noise) in coarse meshes. In our formulation we release the hypothesis of constant fibre angle within each element. In fact, in order to obtain a more accurate description of the variability of the stiffness, the matrix  $\mathbf{C}_\rho^{-1}$  of Eq.(5) can vary through the element domain. In particular, using the Gauss technique, we compute the integrals on a grid  $2 \times 2$  assuming that the fibre angle varies across points. Similarly, the variability of the stiffness matrix within each element has been recently considered by Macquart et al. [50] for a VAT beam displacement-based FE, leading to smooth strains and high convergence rate.

Since the solid-shell FE element is directly derived from the 3D continuum and uses the Green strain measure, then the generalised deformation has a simple quadratic dependence from  $\mathbf{d}_e$  and can be written as

$$\boldsymbol{\rho}_e[\mathbf{d}_e] = \left( \mathbf{L}_e + \frac{1}{2} \mathbf{Q}_e[\mathbf{d}_e] \right) \mathbf{d}_e \quad (6)$$

where  $\mathbf{L}_e$  and  $\mathbf{Q}_e$  are strain interpolation matrices, respectively constant and linear with respect to  $\mathbf{d}_e$  and their expression can be found in [48]. In this way the strain energy, Eq.(4), has only a third order polynomial dependence on the finite element parameters  $\mathbf{u}_e = \{\boldsymbol{\beta}_e, \mathbf{d}_e\}$ .

Note that, exploiting the linear dependence of  $\mathbf{Q}_e[\mathbf{d}_e]$  on  $\mathbf{d}_e$  and its symmetry, we have

$$\begin{aligned} \mathbf{Q}_e[\mathbf{d}_{e1}] \mathbf{d}_{e2} &= \mathbf{Q}_e[\mathbf{d}_{e2}] \mathbf{d}_{e1} \\ \boldsymbol{\beta}_e^T \mathbf{Q}_e[\mathbf{d}_{e1}] \mathbf{d}_{e2} &= \mathbf{d}_{e1}^T \boldsymbol{\Gamma}_e[\boldsymbol{\beta}_e] \mathbf{d}_{e2} \end{aligned}, \quad \forall \mathbf{d}_{e1}, \mathbf{d}_{e2} \quad (7)$$

where the symmetric matrix  $\boldsymbol{\Gamma}_e$  is so defined

$$\boldsymbol{\Gamma}_e[\boldsymbol{\beta}_e] = \frac{\partial^2}{\partial \mathbf{d}_e^2} (\mathbf{t}_e^T \boldsymbol{\rho}_e[\mathbf{d}_e])$$

### 2.1.1. Strain energy variations

Eq.(4) furnishes the strain energy as an algebraic nonlinear function of the element vector

$$\mathbf{u}_e = \begin{bmatrix} \boldsymbol{\beta}_e \\ \mathbf{d}_e \end{bmatrix} \quad (8)$$

related to the global vector  $\mathbf{u} = [\boldsymbol{\beta}, \mathbf{d}]^T$ , collecting all the DOFs of the FE assemblage, through the relation

$$\mathbf{u}_e = \mathcal{A}_e \mathbf{u} \quad (9)$$

where matrix  $\mathcal{A}_e$  contains the link between the elements.

From now on  $\delta u_i$  denotes a generic variation of the configuration field  $u$  and  $\delta \mathbf{u}_i$  the corresponding FE vector. Letting  $\delta \mathbf{u}_{ei} = [\delta \boldsymbol{\beta}_{ei}, \delta \mathbf{d}_{ei}]^T$  the element vector corresponding to  $\delta \mathbf{u}_i$ , the first variation of the strain energy (4) is

$$\Phi'_e \delta u_1 = \begin{bmatrix} \delta \boldsymbol{\beta}_{e1} \\ \delta \mathbf{d}_{e1} \end{bmatrix}^T \begin{bmatrix} \mathbf{s}_{e\beta} \\ \mathbf{s}_{ed} \end{bmatrix} = \delta \mathbf{u}_{e1}^T \mathbf{s}_e[\mathbf{u}_e] \quad (10a)$$

where  $\mathbf{s}_e[\mathbf{u}_e]$  is the *internal force vector* of the element and

$$\begin{cases} \mathbf{s}_{e\beta} = (\mathbf{L}_e + \frac{1}{2} \mathbf{Q}_e[\mathbf{d}_e]) \mathbf{d}_e - \mathbf{H}_e \boldsymbol{\beta}_e \\ \mathbf{s}_{ed} = \mathbf{B}_e[\mathbf{d}_e]^T \boldsymbol{\beta}_e \end{cases} \quad (10b)$$

with  $\mathbf{B}_e[\mathbf{d}_e] = \mathbf{L}_e + \mathbf{Q}_e[\mathbf{d}_e]$ .

Exploiting Eqs.(7), the second strain energy variation is

$$\begin{aligned} \Phi''_e \delta u_1 \delta u_2 &= \begin{bmatrix} \delta \boldsymbol{\beta}_{e1} \\ \delta \mathbf{d}_{e1} \end{bmatrix}^T \begin{bmatrix} -\mathbf{H}_e & \mathbf{B}_e[\mathbf{d}_e] \\ \mathbf{B}_e[\mathbf{d}_e]^T & \boldsymbol{\Gamma}_e[\boldsymbol{\beta}_e] \end{bmatrix} \begin{bmatrix} \delta \boldsymbol{\beta}_{e2} \\ \delta \mathbf{d}_{e2} \end{bmatrix} \\ &= \delta \mathbf{u}_{e1}^T (\mathbf{K}_{0e} + \mathbf{K}_{1e}[\mathbf{u}_e]) \delta \mathbf{u}_{e2} \end{aligned} \quad (10c)$$

that provides the element tangent stiffness matrix  $\mathbf{K}_e[\mathbf{u}_e] = \mathbf{K}_{0e} + \mathbf{K}_{1e}[\mathbf{u}_e]$  as a sum of the linear elastic contribution  $\mathbf{K}_{0e}$  and the geometric matrix  $\mathbf{K}_{1e}[\mathbf{u}_e]$  implicitly defined in Eq.(10c).

Lastly the third variation becomes

$$\begin{aligned} \Phi'''_e \delta u_1 \delta u_2 \delta u_3 &= \left\{ \delta \boldsymbol{\beta}_{e1}^T \mathbf{Q}[\delta \mathbf{d}_{e3}] \delta \mathbf{d}_{e2} + \delta \boldsymbol{\beta}_{e2}^T \mathbf{Q}[\delta \mathbf{d}_{e3}] \delta \mathbf{d}_{e1} \right. \\ &\quad \left. + \delta \boldsymbol{\beta}_{e3}^T \mathbf{Q}[\delta \mathbf{d}_{e2}] \delta \mathbf{d}_{e1} \right\} \\ &= \begin{bmatrix} \delta \boldsymbol{\beta}_{e1} \\ \delta \mathbf{d}_{e1} \end{bmatrix}^T \begin{bmatrix} \mathbf{s}''_{e\beta}[\delta \mathbf{d}_{e2}, \delta \mathbf{d}_{e3}] \\ \mathbf{s}''_{ed}[\delta \mathbf{d}_{e2}, \delta \mathbf{d}_{e3}] \end{bmatrix} \end{aligned} \quad (10d)$$

where

$$\begin{cases} \mathbf{s}''_{e\beta}[\delta \mathbf{d}_{e2}, \delta \mathbf{d}_{e3}] = \mathbf{Q}[\delta \mathbf{d}_{e3}] \delta \mathbf{d}_{e2} \\ \mathbf{s}''_{ed}[\delta \mathbf{d}_{e2}, \delta \mathbf{d}_{e3}] = \mathbf{Q}[\delta \mathbf{d}_{e3}]^T \delta \boldsymbol{\beta}_{e2} + \mathbf{Q}[\delta \mathbf{d}_{e2}]^T \delta \boldsymbol{\beta}_{e3} \end{cases} \quad (10e)$$

Eqs. (10d) and (10e) furnish the secondary forces element vector as

$$\Phi'''_e \delta u_1 \delta u_2 \delta u_3 = \delta \mathbf{u}_{e1}^T \mathbf{s}''_e[\delta \mathbf{u}_{e2}, \delta \mathbf{u}_{e3}] \quad (10f)$$

Finally Eq.(1) and (9) allow the evaluation of the quantities of the whole assemblage

$$\mathbf{y} = \sum_e \mathcal{A}_e^T \mathbf{y}_e, \quad \mathbf{Y} = \sum_e \mathcal{A}_e^T \mathbf{Y}_e \mathcal{A}_e, \quad (11)$$

with  $\mathbf{y}_e$  and  $\mathbf{Y}_e$  representing general FE vectors and matrices respectively, while  $\mathbf{y}$  and  $\mathbf{Y}$  are the corresponding global quantities.

### 3. Koiter's method for solid-shell

On the basis of the FE environment described in Sec.2, the system of equilibrium equations can be written as

$$\mathbf{r}[\lambda, \mathbf{u}] = \mathbf{s}[\mathbf{u}] - \lambda \hat{\mathbf{p}} = \mathbf{0} \quad (12)$$

where  $\mathbf{r}$  is the residual vector,  $\mathbf{s}$  is the internal force vector,  $\hat{\mathbf{p}}$  is the reference load vector,  $\mathbf{u}$  are the FE variables and  $\lambda$  is the load factor. Equation (12) represents a nonlinear problem which defines the equilibrium

path of the structure in the  $\mathbf{u} - \lambda$  space. The nonlinear problem described by Eq.(12) can be iteratively solved using arc-length strategies as [24, 25]. However, in the following we briefly illustrate the main steps performed by Koiter's method to evaluate an estimate of its solution. As the structural problem is discretised using the hybrid solid-shell FE described in Sec.2, the strain energy has a cubic polynomial dependence on the configuration variables. This consideration has positive implications regarding both the efficiency and the accuracy of the method [38].

The description of Koiter's algorithm is organised into two parts. First, the construction of the ROM of the perfect structure is discussed, i.e. structure without any imperfection. Then, it is shown how the ROM for an imperfect structure is obtained. In particular, this is done by adding some terms, related to the imperfection, to the ROM of the perfect structure. This a-posteriori means of accounting for imperfections makes it possible to perform imperfection sensitivity analyses efficiently [30, 31]. Further details on Koiter's algorithm for hybrid solid-shell can be found elsewhere [48, 51].

### 3.1. Perfect structure analysis

The construction of the ROM for the perfect structure consists of the following steps:

1. The initial path tangent  $\hat{\mathbf{u}}$  is evaluated by solving the linear system

$$\mathbf{K}_0 \hat{\mathbf{u}} = \hat{\mathbf{p}} \quad (13a)$$

where  $\mathbf{K}_0 \equiv \mathbf{K}[\mathbf{0}]$  is the tangent matrix evaluated at the rest configuration.

2. A restricted number  $m$  of linearised buckling modes and loads can be obtained by the following eigenvalue problem

$$\mathbf{K}[\lambda] \dot{\mathbf{v}} = (\mathbf{K}_0 + \lambda \mathbf{K}_1[\hat{\mathbf{u}}]) \dot{\mathbf{v}} = \mathbf{0} \quad (13b)$$

where  $\mathbf{K}_1[\hat{\mathbf{u}}]$  is the geometric matrix.

3. The  $m \times (m + 1)/2$  quadratic corrections  $\mathbf{w}_{ij}$ ,  $\hat{\mathbf{w}} \in \mathcal{W}$  are obtained, adopting a Lagrangian multiplier approach (see [48]), by the solution of the linear systems ( $i = 1 \dots m, j = i \dots m$ )

$$\begin{cases} \mathbf{K}_b \mathbf{w}_{ij} + \mathbf{p}_{ij} = \mathbf{0} \\ \mathbf{w}_{ij}^T \mathbf{K}_1[\hat{\mathbf{u}}] \dot{\mathbf{v}}_k = 0, \quad k = 1 \dots m \\ \mathbf{K}_b \hat{\mathbf{w}} + \mathbf{p}_{00} = \mathbf{0} \\ \hat{\mathbf{w}}^T \mathbf{K}_1[\hat{\mathbf{u}}] \hat{\mathbf{u}} = 0. \end{cases} \quad (13c)$$

where  $\mathbf{K}_b = \mathbf{K}[\lambda_b]$  and  $\lambda_b$  is a representative value of the buckling loads cluster, usually chosen as the first linearised buckling load, and

$$\mathbf{p}_{ij} = \mathbf{K}_1[\dot{\mathbf{v}}_i] \dot{\mathbf{v}}_i, \quad \mathbf{p}_{00} = \mathbf{K}_1[\hat{\mathbf{u}}] \hat{\mathbf{u}}.$$

4. The FE variables can be expressed as functions of  $\lambda$  and modal amplitudes  $\xi_i$  assuming the following form

$$\mathbf{u}_d[\lambda, \xi_i] = \lambda \hat{\mathbf{u}} + \sum_i \xi_i \dot{\mathbf{v}}_i + \frac{1}{2} \sum_{ij} \xi_i \xi_j \mathbf{w}_{ij} + \frac{1}{2} \lambda^2 \hat{\mathbf{w}} \quad (13d)$$

that defines the ROM of the perfect structure.

5. The reduced system of equations can now be obtained by projecting the equations  $\mathbf{r}[\lambda, \mathbf{u}_d] = \mathbf{0}$  in directions  $\dot{\mathbf{v}}_i$ ,  $i = 1 \dots m$ , and maintaining the terms up to the 3rd order in  $\xi$  as

$$\begin{aligned} r_k[\lambda, \xi_i] = & \mu_k[\lambda] + (\lambda_k - \lambda) \xi_k - \frac{1}{2} \lambda^2 \sum_{i=1}^m \xi_i \mathcal{C}_{ik} + \frac{1}{2} \sum_{i,j=1}^m \xi_i \xi_j \mathcal{A}_{ijk} \\ & + \frac{1}{6} \sum_{i,j,h=1}^m \xi_i \xi_j \xi_h \mathcal{B}_{ijhk} = 0, \quad k = 1 \dots m \end{aligned} \quad (13e)$$

where the coefficients  $\mathcal{A}_{ijk}$ ,  $\mathcal{C}_{ik}$ ,  $\mathcal{B}_{ijhk}$  and  $\mu_k[\lambda]$  are scalar quantities evaluated as the sum of element contributions of the strain energy variations evaluated in section 2.1.1

$$\begin{aligned}\mathcal{A}_{ijk} &= \Phi''' \dot{v}_i \dot{v}_j \dot{v}_k \\ \mathcal{C}_{ik} &= \Phi_b'' \hat{w} w_{ik} \\ \mathcal{B}_{ijhk} &= -\Phi_b'' (w_{ij} w_{hk} + w_{ih} w_{jk} + w_{ik} w_{jh}) \\ \mu_k[\lambda] &= \frac{1}{2} \lambda^2 \Phi''' \hat{u}^2 \dot{v}_k,\end{aligned}\tag{13f}$$

where  $\Phi_b''$  is the second strain energy variation evaluated for  $\lambda = \lambda_b$ . Eqs.(13e) are an algebraic nonlinear system of  $m$  equations in the  $m + 1$  variables  $\lambda, \xi_1 \dots \xi_m$  that, due to the small size of the system, can be efficiently solved using specialised variants of the arc-length scheme.

Once Eq.(13e) is solved, the equilibrium path in terms of FE variables can be recovered by substituting  $\lambda, \xi_1 \dots \xi_m$  into Eq.(13d).

### 3.2. Imperfection sensitivity analysis

A remarkable advantage for analysing a slender structure with Koiter's method resides in the possibility of performing an efficient and robust imperfection sensitivity analysis. In fact, once the nonlinear system of Eq.(13e) has been resolved for the perfect structure, we can study the imperfect structure by only perturbing a posteriori the system (13e), or rather by adding to it the imperfection term  $\tilde{\mu}_k$ . Therefore, the system of Eq.(13e) becomes

$$r_k + \tilde{\mu}_k = 0.\tag{14}$$

This means that all the scalar coefficients of the system (14) are still those evaluated for the perfect structure and the analysis of a new geometrical imperfection needs simply to update  $\tilde{\mu}_k$  and re-solve the system given by Eq.(14). In this manner, we can test many kinds of imperfections in a few seconds (i.e. thousands of imperfections). Evidently, for a given structure, it is impractical to obtain the same quantity of information in so a short timeframe if the nonlinear analysis is performed with a path-following approach.

For the evaluation of  $\tilde{\mu}_k$  two strategies have been proposed over the years [51]. The first one evaluates the ROM of the imperfect structure as

$$\mathbf{u}_d[\lambda, \xi_i] = \tilde{\mathbf{u}} + \lambda \hat{\mathbf{u}} + \sum_i \xi_i \hat{\mathbf{v}}_i + \frac{1}{2} \sum_{ij} \xi_i \xi_j \mathbf{w}_{ij} + \frac{1}{2} \lambda^2 \hat{\mathbf{w}}.\tag{15}$$

The imperfection term  $\tilde{\mu}_k$  is evaluated as

$$\tilde{\mu}_k = \lambda \Phi''' \hat{u} \tilde{v}_k.\tag{16}$$

This representation has been used in several works [31, 32, 42] and gives good results at a practically insignificant computational cost. Some inaccuracy has only been observed when analysing structures characterised by a strongly nonlinear pre-critical behaviour and with large amplitude imperfections, which likely alter the pre-buckling stresses and so are no longer strictly imperfections, as they may increase as well as decrease buckling loads depending on the nature of the load redistribution. Therefore, Garcea et al. [51] proposed a way to extend the validity of the formulation at a little higher computational cost. However, since we are considering the optimisation of a well-behaved structure, the first strategy is employed.

In this work, we assume the shape of the geometrical imperfection to be an initial displacement  $\tilde{\mathbf{u}}$ , which is defined as linear combination of known shapes  $\tilde{\mathbf{u}}_i$  and scalar values  $\tilde{\xi}_i$ ,

$$\tilde{\mathbf{u}} = \sum_{i=1}^n \tilde{\xi}_i \tilde{\mathbf{u}}_i.\tag{17}$$

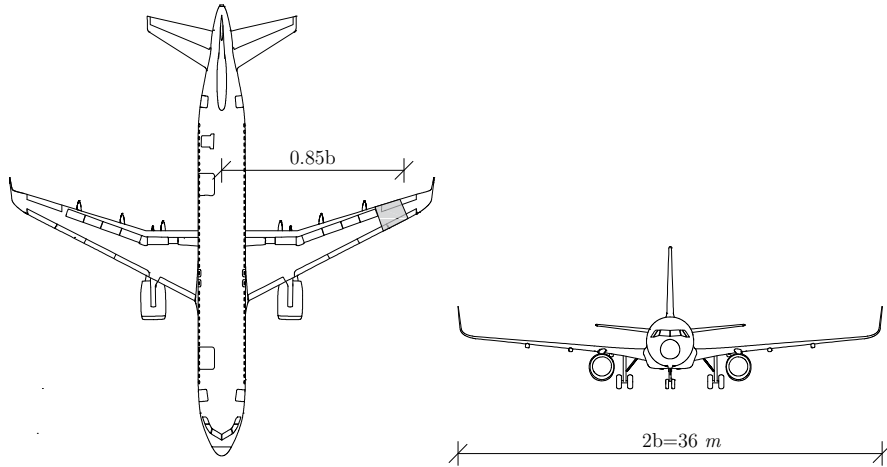


Figure 1: Wingbox position on the aircraft.

#### 4. Optimisation of a composite VAT wingbox

In this section, the optimisation strategy of the VAT composite wingbox proposed by Oliveri et al. [2] is illustrated. At first, the wingbox is described. Then, we present the Koiter asymptotic approach coupled with two stochastic optimisation strategies, namely MCA and GA.

##### 4.1. VAT wingbox

The wingbox under consideration is representative of a medium-range civil aircraft having a maximum take-off mass of  $75t$  and a wingspan of  $2b = 36m$  (see Fig.1). In particular, Oliveri et al. [2] designed the wingbox assuming that it is located at about the 85% of the aircraft's half wingspan between two ribs.

The cross-sectional dimensions have been designed considering a linear-elastic beam model with a Quasi Isotropic (QI) composite layup under an elliptical load distribution that simulates the load during cruise [43]. During the design process, for each cross-section of the beam, the second moment of area along the  $X$  axes (see Fig.(2)) has been assumed to be proportional to the bending moment along the  $X$  axes. Therefore, by imposing the deflection of the tip of the wing to be equal to a design value (i.e. a percentage of  $b$ ), it was possible to evaluate the forces and moments acting on a generic cross-section of the wing [2].

The main geometrical quantities of the wingbox under consideration are shown in Fig.3. More details regarding the geometry and their design process can be found in Oliveri et al. [2]. In Fig.4 the loading and boundary conditions of the wingbox are shown. In particular, the wingbox is considered to be loaded on one end by a shear force  $F_A = 23.8kN$  and a flexural moment  $M_A = 14.28kNm$ , while the opposite side is fully clamped.

The layup of the wingbox was chosen to perform well against buckling. It is reported in Table 1 and denoted by  $SS_0$  in the following. The angle  $\theta$  is measured in the direction of the local tangent at the surface ( $\mathbf{e}_3$ ) with respect to the direction  $\mathbf{e}_1$ , referring to the local reference system of each panel shown in Fig.2. It has been assigned such that the direction  $\mathbf{e}_1$  aligns with the direction  $\mathbf{Y}$  of the global system and  $\mathbf{e}_3$  goes from the inside out. The layups of the variable angle tow panels are expressed in according to the notation of Gürdal and Olmedo [4]. The material properties are given in Table 2 and the thickness of each layer is  $0.1875mm$ . As shown in Table 1, the skin comprises eleven layers, while four additional  $0^\circ$  layers have been added to the spar webs for increasing their stiffness. The wingbox has been designed to keep the principal strains under a limit value, namely  $\varepsilon_{lim} = 2500\mu\epsilon$ .

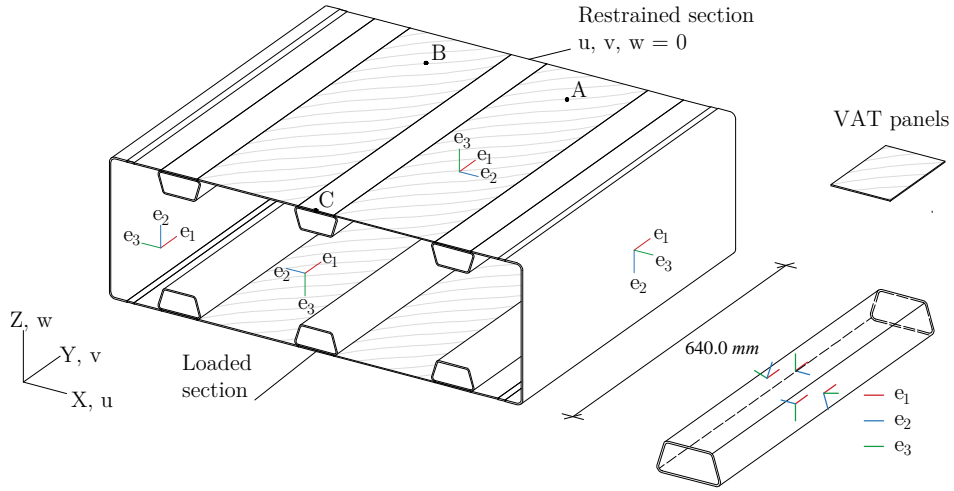


Figure 2: Geometry, loading and boundary conditions of the wingbox.

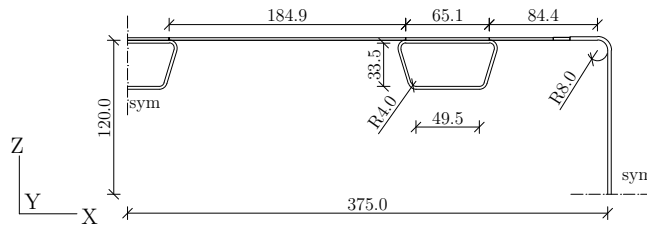


Figure 3: Detailed view of the cross-section of the wingbox. All the lengths are expressed in *mm*.

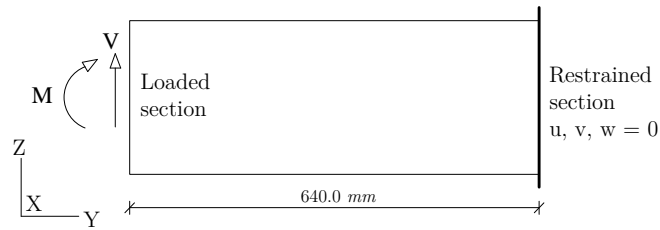


Figure 4: Loads and boundary conditions applied at the two end sections of the wingbox.

Table 1: Layup  $SS_0$  of the wingbox.

Skin bay	Skin	Stiffener	Spar web
$90/[(0 \pm \langle 52 35 \rangle)/0 / \pm 45]_S$	$90/[\pm 35/0 / \pm 45]_S$	$[90/45/0_2 / - 45/0]_S$	$90/[\pm 35/0_3 / \pm 45]_S$

Table 2: Material properties.

$E_1[GPa]$	$E_2[GPa]$	$G_{12}[GPa]$	$\nu_{12}$
135.00	7.54	5.00	0.30

Table 3: Parametric fibre paths used in the optimisation problem.

Skin bay	Skin	Stiffener	Spar web
$90/[(0 \pm \langle \vartheta_1   \vartheta_2 \rangle)/0/(0 \pm \langle \vartheta_4   \vartheta_3 \rangle)]_S$	$90/[\pm \vartheta_2/0/ \pm \vartheta_3]_S$	$[90/45/0_2/ - 45/0]_S$	$90/[(0 \pm \langle \vartheta_5   \vartheta_2 \rangle)/0_3/(0 \pm \langle \vartheta_6   \vartheta_3 \rangle)]_S$

#### 4.2. Optimisation strategy

The goal of the current optimisation study is to minimise the out-of-plane displacement of the wingbox under a design load. In fact, the most notable effect observed in the wingbox in the postbuckling regime is an increasing transverse displacement of the skin panels in compression. Consequently, its minimisation improves the postbuckling performances, as shown by Raju et al. [23]. The maximum out-of-plane displacement is denoted by  $w_{c,max}$  and is measured at the points where the maximum amplitude of the buckling modes occurs. The design load is 1.2 times the applied load.

The optimisation variables are the angles of the stacking sequence, denoted as  $\boldsymbol{\vartheta} = [\vartheta_1, \dots, \vartheta_6]$ . The first layer of  $90^\circ$  is kept constant due to manufacturing need [2]. The optimisation is based on a fibre path parameterisation according to Gurdal and Olmedo [4]. Table 3 shows the parametric layup. The fibre angle of skin and web is compatible at the corners, guaranteeing the continuity of the fibre path. The angles are constrained to integer values and their domain is defined from  $-90^\circ$  to  $90^\circ$ .

Strains and tip displacement are constrained to be less than  $\varepsilon_{lim} = 2500\mu\epsilon$ , and  $w_{lim} = w_{QI,max} = 2.38\text{ mm}$ , respectively. These constraints are included in the optimisation process by assigning a penalty value to the objective function if any limit is exceeded

$$f(\boldsymbol{\vartheta}) = \begin{cases} \frac{|w_{max}|}{w_{lim}} + c_1 & \text{if } |w_{max}| > w_{lim} \\ \frac{|\varepsilon_p|}{\varepsilon_{lim}} + c_2 & \text{if } |\varepsilon_p| > \varepsilon_{lim} \\ |w_{c,max}| & \text{otherwise.} \end{cases} \quad (18)$$

where  $w_{max}$  is the tip displacement,  $\varepsilon_p$  is the maximum principal strain,  $c_1$  and  $c_2$  are the penalty constants. If both the limits are exceeded, the highest value evaluated by Eq.(18) is applied.

The VAT steering radius is constrained to exceed a minimum value to guarantee manufacturability. The limit amplitude is  $R_{lim} = 400\text{ mm}$ , according to results previously presented [44]. Consequently, nonlinear inequality constraints are included in the optimisation

$$c_r(T_{0,v}, T_{1,v}) = R_{lim} - \frac{L_v}{|\cos(T_{0,v}) - \cos(T_{1,v})|} \leq 0; \quad (19)$$

where  $v$  is defined from 1 to the number of VAT panels  $n_{vat}$ ,  $L_v$  is the characteristic length of the  $v$ th panel as defined in the VAT notation and  $T_{0,v}$ ,  $T_{1,v}$  are the angles at the centre and at the end of the panel, respectively.

Finally, the optimisation problem can be stated as

$$\begin{aligned} & \underset{\boldsymbol{\vartheta}}{\text{minimise}} && f(\boldsymbol{\vartheta}) \\ & \text{subject to} && c_r(T_{0,v}, T_{1,v}) \leq 0, \quad v = 1 \dots n_{vat} \\ & && \vartheta_i \in \mathcal{N} \\ & && -90^\circ \leq \vartheta_i \leq 90^\circ, \quad i = 1 \dots 6 \end{aligned} \quad (20)$$

The nonlinear displacements and strains are evaluated using Koiter's method.

#### 4.3. The "worst-case" imperfection shape

In Sec.3.2, it was shown that Koiter's method can provide the equilibrium path of a structure with a geometrical imperfection expressed as a linear combinations of known shapes. We choose to include

imperfections that are combinations of the buckling modes used in the asymptotic expansion and then, referring to Eq.(17), we have

$$\bar{\mathbf{u}}_i = \dot{\mathbf{v}}_i, \quad i = 1 \dots m. \quad (21)$$

The values of the scalars  $\tilde{\xi}_i$  of Eq.(17) can vary, while the maximum amplitude of each imperfection is fixed as

$$\max |\tilde{\mathbf{u}}| = \tilde{u}_{max}. \quad (22)$$

To the best of our knowledge, no data are available on the maximum imperfection amplitude introduced by the technology used for manufacturing the wingbox [2]. Therefore we have chosen to use a small imperfection, namely  $\tilde{u}_{max}$  is equal to 1/50 of the skin thickness, just to assess the stability of the postbuckling behaviour. More precise simulations can be performed once data on measured imperfections are available.

For a given value of  $\vartheta$ , the equilibrium path depends on the imperfections. Among all possible imperfections obtained by varying scalars  $\tilde{\xi}_i$ , the "worst-case" imperfection shape is defined as the one that gives the maximum value of the postbuckling out-of-plane displacement. Finding the "worst-case" imperfection shape represents a sub-optimisation problem, which is solved for each value of  $\vartheta$ . Its solution is obtained with a simple Monte Carlo method [30, 42].

#### 4.4. Optimisation algorithms

Notable success has been made with gradient based optimisers using lamination parameters [52–54] which allow many layers to be optimised independently from each other. However, the optimisation problem in its present form is highly nonlinear and non-convex. In this case, stochastic strategies are a suitable solution method. In fact, they are able to easily find many near optimal solutions and require no information on the gradient, but do require many analyses. Moreover, they are insensitive to the complexity of the design space. In particular, we use a standard integer-based GA [55] and a modified version of MCA [42]. In GA the inequality constraints are efficiently handled with a penalty function approach that does not require that the penalty parameter is explicitly set [56]. In the next section, the MCA is briefly described.

##### 4.4.1. The Monte Carlo Algorithm (MCA)

The Monte Carlo random search simulation is based on two stages [42]. During the first stage, it generates a random population of  $N_1$  layups and the objective function is evaluated for each of them. The best  $n = n_1$  solutions, identified as being an elite ( $\mathbf{x}_{el}$ ), are selected and represent the starting points of the second stage. This is constructed by a sequence of steps (zoom steps) that try to improve the elite population. For each elite value  $\mathbf{x}_{el}$ , the objective function is evaluated  $N_2$  times at random points defined as

$$\vartheta(j) = \mathbf{x}_{el}(j) + rnd(-R, R)$$

where  $j = 1 \dots n$  denotes the elite value and  $rnd$  is a generator of pseudo random integer values between  $-R$  and  $R$ . The radius  $R$  assumes the value  $R_1$  during the first zoom step and  $R_2$  during the following ones.

At the end of a zoom step,  $n = n_2$  best solutions are selected and represent the elite population of the next step. If convergence is reached the algorithm stops, otherwise a next zoom step is performed.

The algorithm is summarised in the flowchart shown in Fig.5. The values of the parameters of the analysis are reported in Table 4.

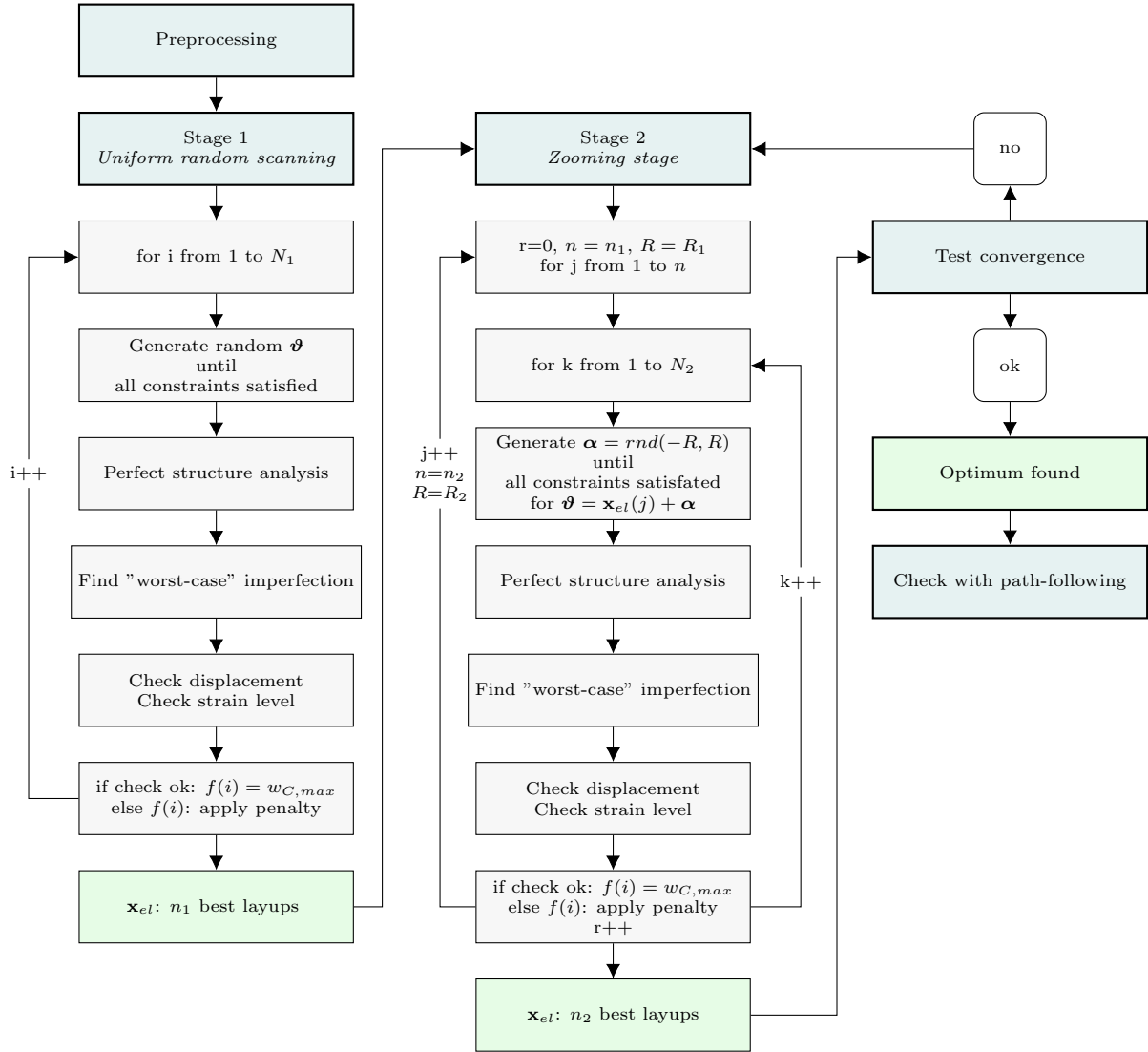


Figure 5: Minimisation of  $f(\boldsymbol{\theta})$  using the MCA.

Table 4: Parameters of the MCA.

property	symbol	value	
		set 1	set 2
initial population	$N_1$	400	800
zoom population	$N_2$	8	10
initial elite	$n_1$	20	30
elite during zooms	$n_2$	5	5
zooms	$N_z$	6	10
first zoom radius	$R_1$	8	10
zoom radius	$R_2$	4	6

Table 5: Buckling loads for the initial stacking sequence (SS<sub>0</sub>).

mode	1	2	3	4	5	6	7	8	9	10	11	12
$\lambda_c$	1.1417	1.1555	1.2017	1.2133	1.4285	1.4385	1.5073	1.5269	1.7076	1.7442	1.8310	1.8734
$\lambda/\lambda_{c,1}$	1.000	1.0121	1.0526	1.0627	1.2512	1.2600	1.3202	1.3374	1.4957	1.5277	1.6037	1.6409

## 5. Numerical results

This section is divided into two parts. First, the manufactured wingbox is analysed with the multi-modal Koiter algorithm summarised in section 3 and a comparison is made with results obtained from a path following analysis using a Riks arc-length algorithm [24]. Then, we show the results of the postbuckling optimisation process and propose different design choices.

### 5.1. Validation of the model

Here, we focus on the postbuckling behaviour of the manufactured wingbox. This stage is useful to validate the FE model and to assess the suitability of Koiter’s method.

The wingbox is discretised using the solid-shell FE shown in Section 2. In addition to simplifying the formulation as shown in Section 3, the use of the solid-shell FE gives other advantages. In fact, due to the 3D description, the connection between the stiffeners and the skin can be modelled without rigid links. Moreover, the continuity of the skin is preserved in the zones of variable thickness, unlike classical shell finite elements that need an offset to define the actual position of the panels.

We first present the results of a linear buckling analysis carried out on the FE model. Then, we perform the geometrically non-linear analysis with Koiter’s method. The results in terms of equilibrium path are compared with those provided by an arc-length strategy. It employs the same FE description used by Koiter so that the differences can only be attributed to the solution algorithm. In addition, so as to exclude errors in the FE model, the results are compared with Abaqus/Standard.

#### 5.1.1. Linear buckling analysis

Converged results for linear buckling are obtained with a mesh of 19560 elements and 110151 DOFs. The first twelve buckling loads are reported in Table 5. The corresponding modes are shown in Fig.6. The first buckling load is  $27.17kN$ , that is in agreement with the result of the static test performed on the wingbox by Zucco et al. [57] who gave the measured value of  $26.10 - 27.20kN$ .

#### 5.1.2. Nonlinear analysis

The nonlinear analysis is performed with Koiter’s algorithm. Figure 7 shows some of the quadratic corrections used by the method. Together with the buckling modes shown in Fig.6 and the linear-elastic solution, they constitute the ROM, as expressed in Eq.(13d). First, we perform a Koiter analysis including only the first buckling mode. The results are reported in Fig.8 where they are compared with the reference solution evaluated by the path following method. While the solution at point A is appropriate, an incorrect solution is obtained at point B. The improving correlation at point B between Koiter’s solution and the path-following method for increasing buckling modes is shown in Fig.9. Figure 10 shows how the solution at point A improves with the first two buckling modes. When the first six modes are included, the solution is practically coincident with that obtained from the path following method. Further increasing the number of modes does not produce a noticeable effect, as shown in Fig.11 for points A and C. Figure 12 shows how the variables of the ROM change when the load increases.

In Fig.13 the solution obtained with Koiter’s method including six buckling modes is compared with the solution provided by two path following analyses. The first one is performed on the same FE model used for Koiter analysis, while the second is obtained using a very fine mesh of shell FE S4R in ABAQUS. Very good agreement between them can be observed.

Finally, deformed shapes at two load levels are reported in Fig.14. They are obtained by three Koiter analyses, using one, two and six modes. They confirm that the solution is not correctly captured with one

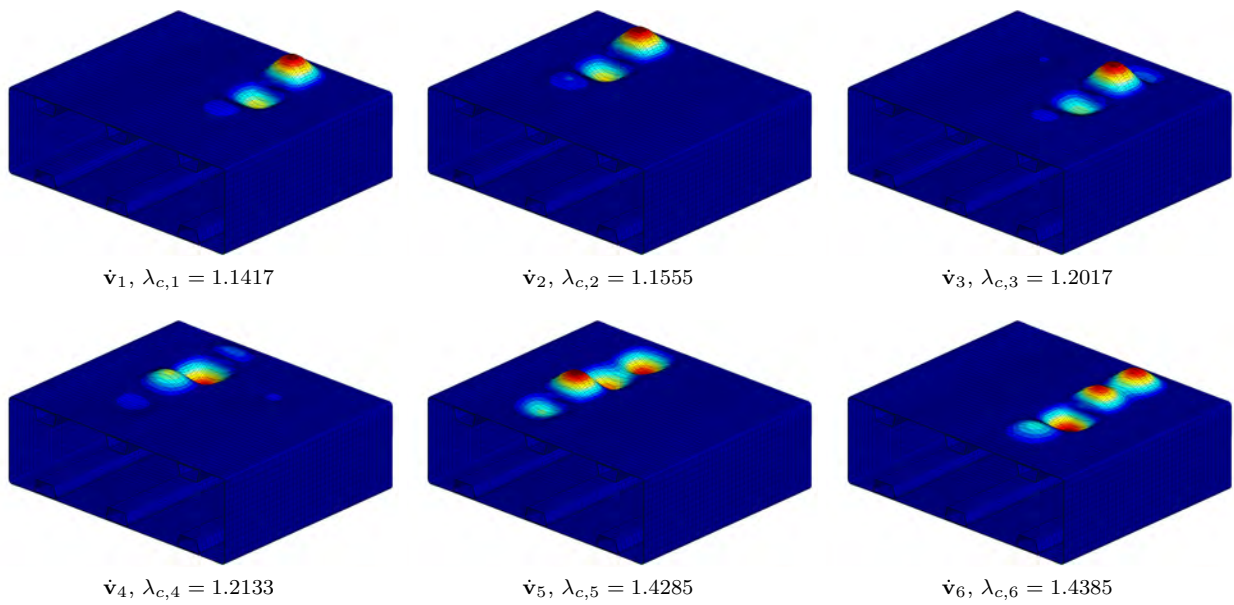


Figure 6: Buckling modes for the initial stacking sequence.

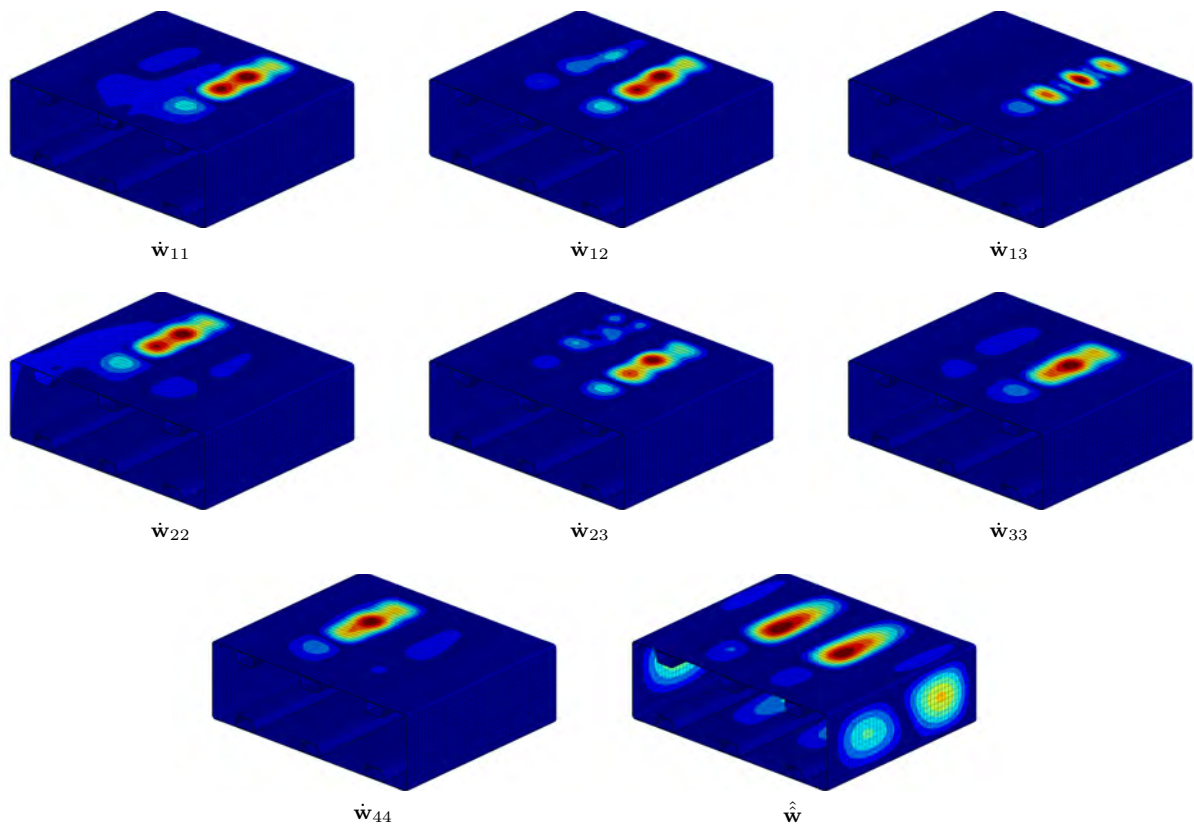


Figure 7: Some of the quadratic correction terms for the  $SS_0$  layup.

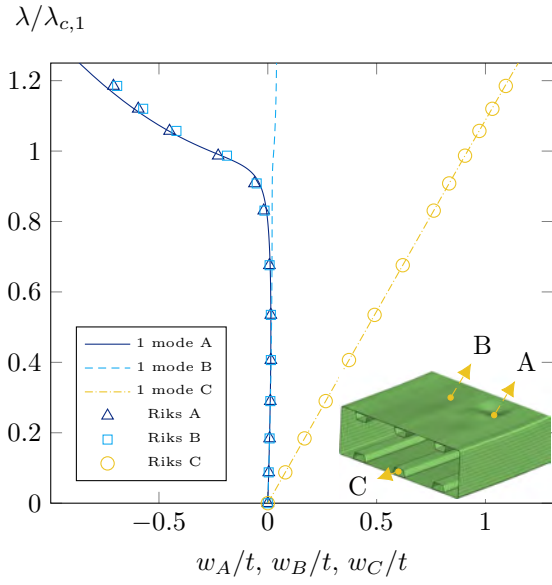


Figure 8: Equilibrium paths for the layup  $SS_0$  with one mode Koiter.

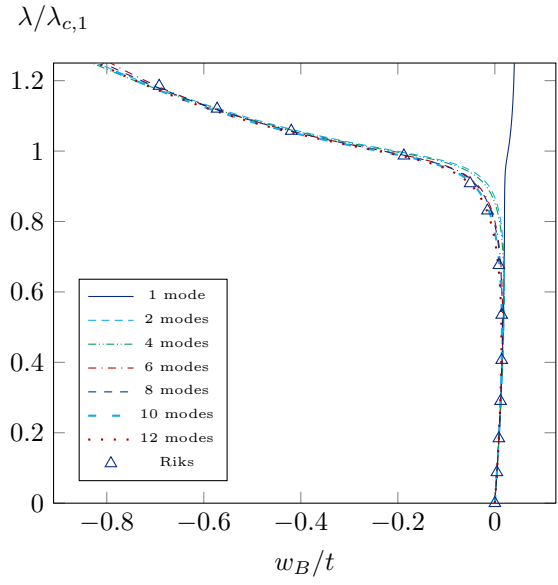


Figure 9: Equilibrium paths at point B for the layup  $SS_0$  using from 1 to 12 buckling modes.

buckling mode, whilst using two modes provides good results over the whole domain. Additionally, the postbuckled out-of-plane displacement is in agreement with that measured from Digital Image Correlation in the buckled region of the wingbox, as shown in Fig.20 and 21 of the work by Zucco et al.[57].

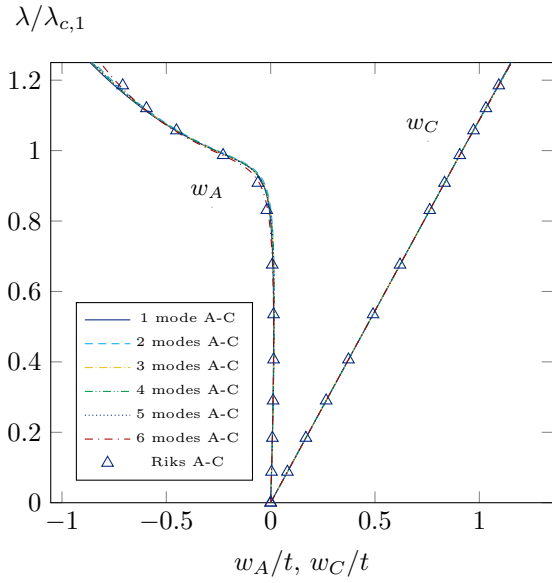


Figure 10: Equilibrium paths for the layup  $SS_0$  using from 1 to 6 buckling modes.

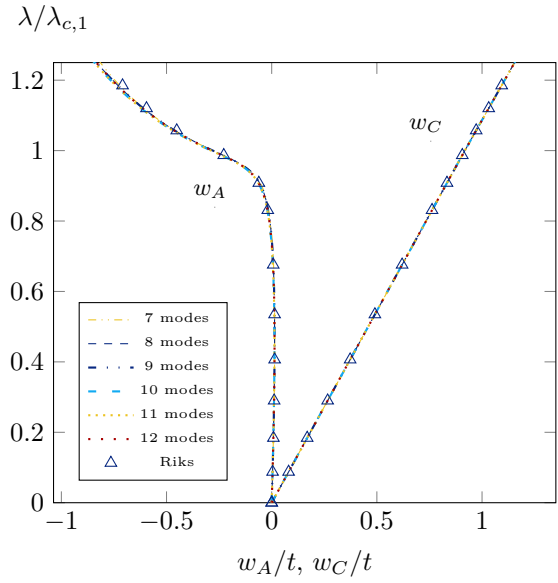


Figure 11: Equilibrium paths for the layup  $SS_0$  using from 7 to 12 buckling modes.

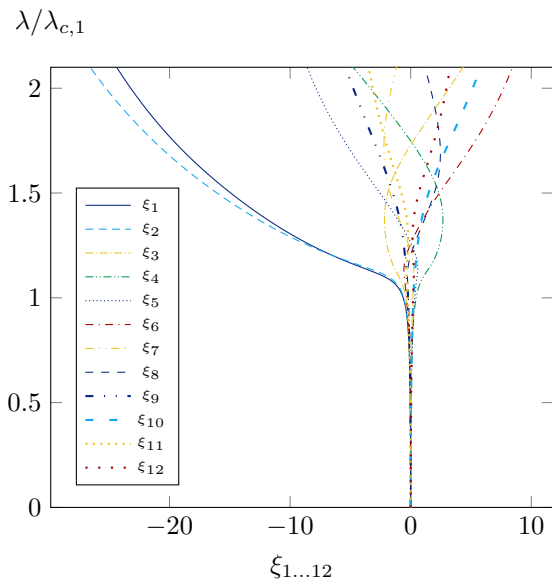


Figure 12: Variables of the ROM with the first 12 buckling modes for the layup  $SS_0$ .

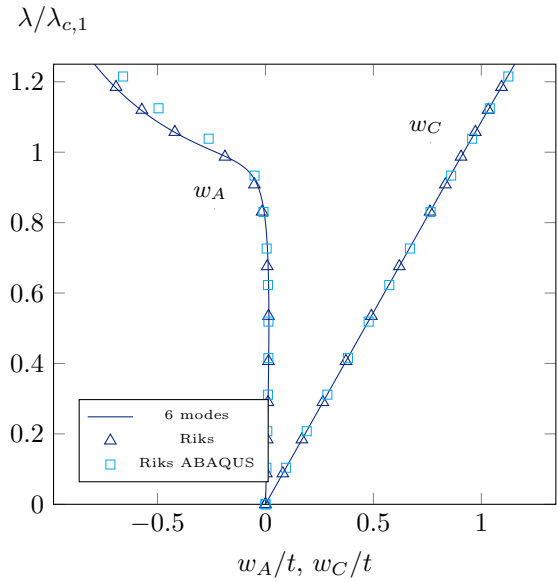


Figure 13: Comparison between the solution provided by Koiter's method and the path following analysis using the solid shell FE and the S4R shell element of ABAQUS, layup  $SS_0$ .

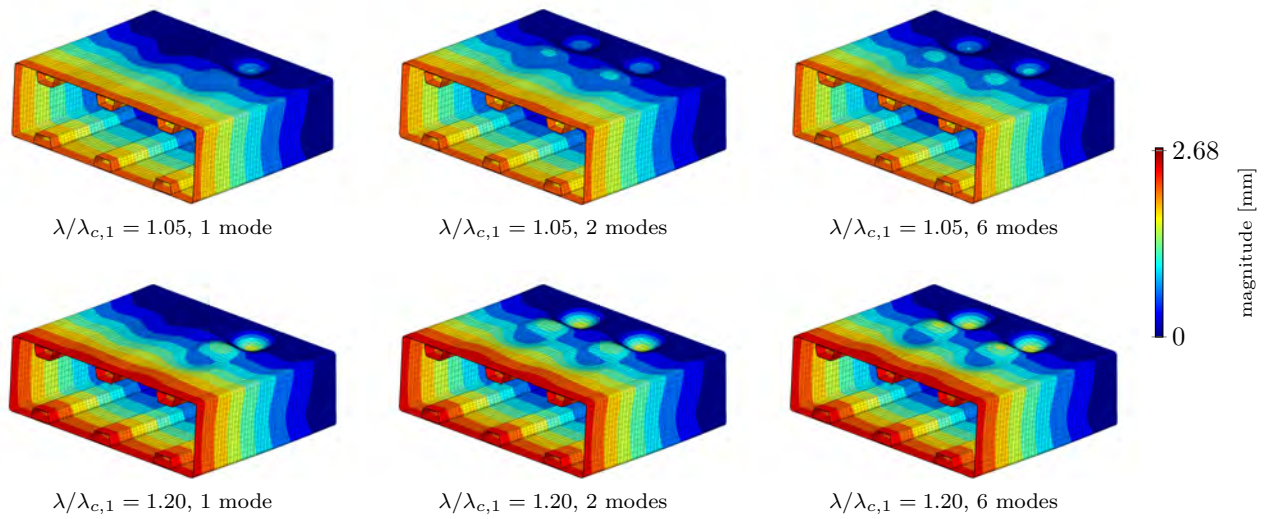


Figure 14: Magnitude of the displacement field for the layup  $SS_0$  at  $\lambda = 1.05$  and  $\lambda = 1.20$  employing the first 1,2 and 6 buckling modes.

Table 6: Stacking sequences  $SS_{A,GA}$  and  $SS_{A,MCA}$  and objective function values.

	Skin bay	Skin	Spar web	$w_{c,max}$
$SS_{A,GA}$	$90/[(0 \pm \langle 53 34 \rangle)/0/(0 \pm \langle 86 77 \rangle)]_S$	$90/[\pm 34/0/\pm 77]_S$	$90/[(0 \pm 34)/0_3/(0 \pm 77)]_S$	0.20
$SS_{A,MCA}$	$90/[(0 \mp \langle 52 34 \rangle)/0/(0 \pm \langle 87 77 \rangle)]_S$	$90/[\mp 34/0/\pm 77]_S$	$90/[(0 \mp 34)/0_3/(0 \pm 77)]_S$	0.20
$SS_{A,MCA}$ (set 2)	$90/[(0 \pm \langle 53 34 \rangle)/0/(0 \mp \langle 90 77 \rangle)]_S$	$90/[\pm 37/0/\mp 77]_S$	$90/[(0 \pm 37)/0_3/(0 \mp 77)]_S$	0.20

## 5.2. Optimisation

The proposed optimisation cases are as follows:

- Case A: in the spar web, the fibre angle is constant and then the number of variables is four. With reference to Table 3,  $\vartheta_5 = \theta_2$ ,  $\vartheta_6 = \theta_3$ ;
- Case B: the problem has six variables active and the displacement limit is reduced, assuming  $w_{lim} = 0.8 \cdot w_{QI,max}$ ;
- Case C: we look for a solution that allows weight to be reduced whilst respecting all constraints.

To make the optimisation process less time consuming, a coarser mesh than the one used in section 5.1 is employed. The results of the optimal solutions are then compared with those obtained with the fine mesh. In Koiter's method, the buckling modes are selected as those corresponding to critical loads that do not exceed 1.3 times the lowest one. This criterion, which is analogous to that employed in the optimisation strategy proposed by Liguori et al. [42], is chosen on the basis of the results of section 5.1.2 regarding the  $SS_0$  layup. The validity of this assumption for the optimal solutions is verified by comparing the equilibrium paths obtained using Koiter's algorithm with those traced using path-following analyses. In the following, the results for all three cases are presented.

### 5.2.1. Case A

First, optimisation is carried out with MCA using the parameter set no.1, as defined in Table 4. The optimal layup is denoted by  $SS_{A,MCA}$ . To assess the convergence of MCA, the analysis is repeated using parameter set no.2 of Table 4. Then, the problem is solved using GA, obtaining the optimal layup denoted by  $SS_{A,GA}$ . The population has 40 individuals and the crossover fraction of each generation is 0.7. The optimal fibre paths and objective function values are shown in Table 6. It is possible to observe that  $w_{c,max}$  remains the same, whilst the value of the optimisation variables slightly changes.

The equilibrium paths for different layups are shown in Fig.15. They are plotted at the point where displacement  $w_{c,max}$  is a maximum, and at point C. In addition, in Fig.16 the equilibrium path of  $SS_{A,GA}$  is compared with those obtained by an arc-length method and with the finer mesh, obtaining good agreement.

Figure 17 shows the map of the principal strains at the design load. They are normalised with respect to the strain limit. The optimised structures have a more uniform distribution of the strains and the maximum value is lower. In particular, the ratio between the maximum principal strain  $|\varepsilon_p|$  and the limit strain  $\varepsilon_{lim}$  is 0.93 for the initial configuration and 0.90 for the optimised ones. Additionally, Fig.18 shows the deformed configurations at the design load. The layup  $SS_0$  is globally stiffer than the optimised ones, even though in  $SS_{A,GA}$  and  $SS_{C,MCA}$  almost no buckling phenomena can be observed. Finally, Fig.19 shows the convergence of the two algorithms. It highlights how the minimum of the objective function changes with increasing function evaluations. In particular, the methods converge to a similar minimum values but, for the problem under consideration and analysis setups, the MCA provides a good estimate with fewer objective function evaluations. In the next paragraph, we show how the results of the optimisation are influenced by the steering radius.

*Influence of the steering radius.* Manufacturing VAT laminates with small steering radii can be a challenging task. In fact, this increases the probability of defects and the gap-overlap effect [44] and, as a consequence, the actual structure can have a different behaviour with respect to the design model if those imperfections are not taken into account. We now show the influence of different steering radius constraints on the

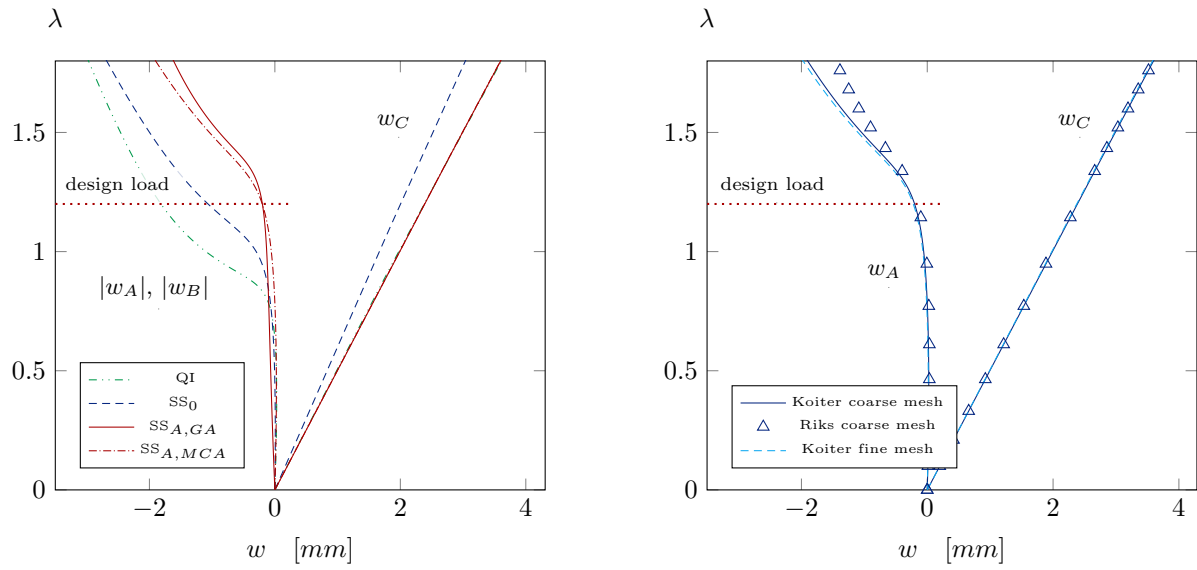


Figure 15: Equilibrium paths of the optimised structures of Figure 16: Solution obtained with Koiter's method and the mesh used during the optimisation process and layout  $SS_{A,MCA}$  compared with that obtained with a path following analysis and with Koiter's algorithm using a finer discretisation.

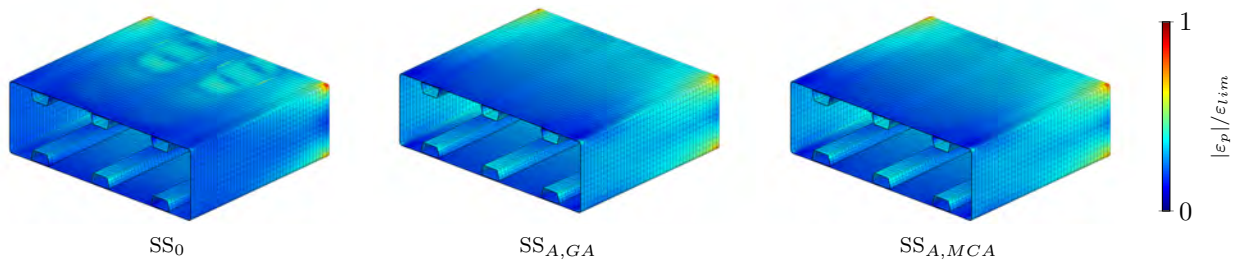


Figure 17: Maximum principal strains normalised for the limit strain of  $2500\mu\epsilon$  at  $\lambda = 1.2$  for the initial and optimised layouts, case A.

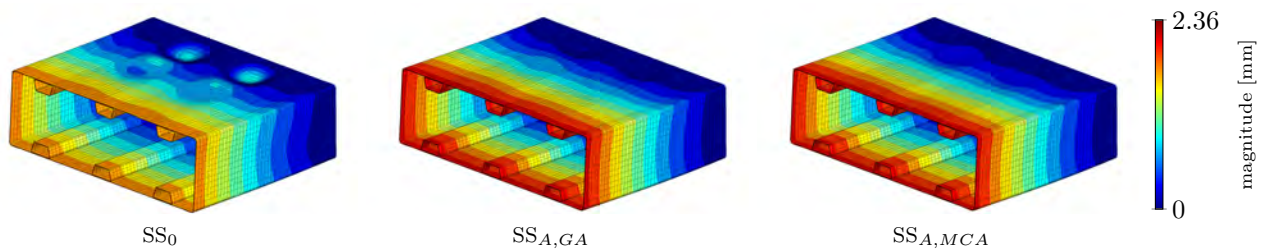


Figure 18: Displacement field at  $\lambda = 1.2$  for the initial and optimised layouts.

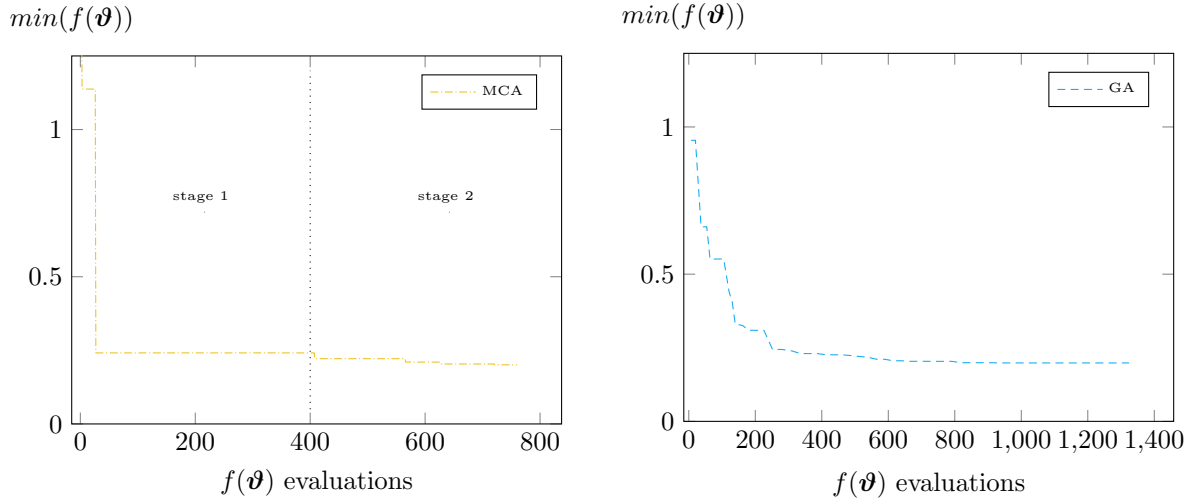


Figure 19: Convergence of MCA (left), and of GA (right), case A.

Table 7: Results of the optimisation problem of case A with different limiting steering radii.  $SS_{2,3}$  and  $SS_{5,6}$  denote the layout of the 2nd, 3rd and of the 5th, 6th layer of the skin, respectively, while with  $R_{2,3}$  and  $R_{5,6}$  the relative steering radii.

$R_{lim}$	200	300	400	600	800	1000	1200	$\infty$
$SS_{2,3}$	$0 \pm \langle 64 26 \rangle$	$0 \pm \langle 57 32 \rangle$	$0 \mp \langle 52 34 \rangle$	$0 \pm \langle 53 41 \rangle$	$0 \pm \langle 51 42 \rangle$	$0 \pm \langle 52 44 \rangle$	$0 \pm \langle 50 44 \rangle$	$\pm 46$
$SS_{5,6}$	$0 \pm \langle 88 71 \rangle$	$0 \pm \langle 84 75 \rangle$	$0 \pm \langle 87 77 \rangle$	$\pm 76$	$0 \pm \langle 76 74 \rangle$	$0 \pm \langle 76 73 \rangle$	$0 \pm \langle 77 74 \rangle$	$\pm 73$
$R_{2,3}$	201	305	433	605	812	1011	1208	$\infty$
$R_{5,6}$	385	726	536	$\infty$	3322	2220	2210	$\infty$
$w_{C,max}$	0.1520	0.1820	0.2018	0.2461	0.2520	0.2602	0.2642	0.3256
$\lambda_{c,1}$	1.5307	1.4763	1.4486	1.4135	1.3919	1.3876	1.3822	1.3435

optimised structures. The optimisation process is repeated for different limiting radii. MCA is employed with parameter set no.1 from Table 4. The same limit is imposed on all VAT layers. In Table 7, the results of these analyses are presented. We show, for each optimised structure with a different minimum radius limit, the stacking sequence of the VAT panels, the actual radii, the value of the objective function and the smallest buckling load. The variation of the optimised displacement with the value of the maximum steering radius is plotted in Fig.20. The results highlight the possibility of considerably enhancing the postbuckling performance by decreasing the VAT steering radius. For example, the steering radius of 200mm leads to a 5.7% higher buckling load and 24.7% decrease in out-of-plane displacement than for a steering radius of 400mm.

### 5.2.2. Case B

The results of case A show how the optimised layouts improve the buckling performances yet reduces the global stiffness. To increase the mean stiffness related to the deflection of the end section, a smaller limit displacement is employed, namely  $w_{lim} = 0.8 \cdot w_{QI,max}$ .

The number of optimisation variables is greater in this case, with a commensurately larger population being used. In particular, a population of 80 individuals is used to optimise the structure using GA and the solution obtained is identified as  $SS_{B,GA}$ . MCA uses parameter set no.2, as defined in Table 4, and the solution provided is labelled  $SS_{B,MCA}$ . The stacking sequences and the displacement  $w_{c,max}$  are reported in Table 8. A graphical representation of a VAT layer of  $SS_{B,GA}$  is given in Fig.21.

The results obtained in terms of equilibrium paths are reported in Fig.22. With respect to the previously obtained layouts, we obtain stiffer structures, even if the buckling performances get slightly worse. Anyway, the postbuckling slope for  $SS_{B,GA}$  and  $SS_{B,MCA}$  is relatively high.

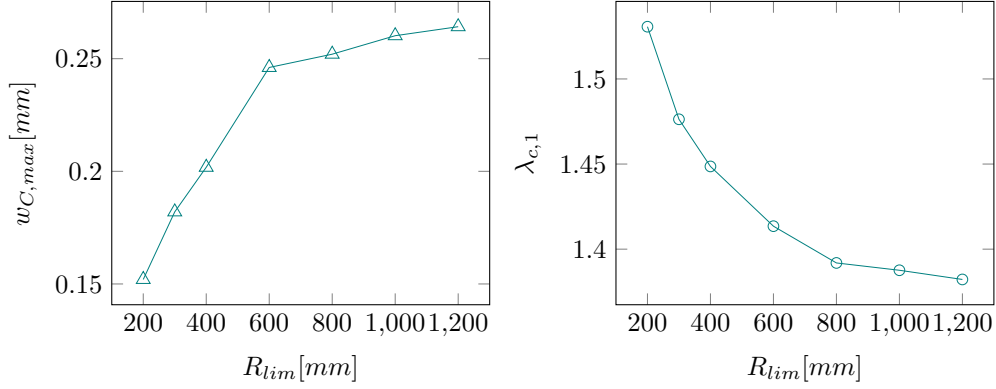


Figure 20: Optimised displacement and buckling load for different values of the maximum steering radius, case A.

Table 8: Stacking sequences  $SS_{B,GA}$  and  $SS_{B,MCA}$  and objective function values.

	Skin bay	Skin	Spar web	$w_{c,max}$
$SS_{B,GA}$	$90/[(0 \pm \langle 57 53 \rangle)/0/(0 \mp \langle 42 13 \rangle)]_S$	$90/[\pm 53/0/\mp 13]_S$	$90/[(0 \pm \langle 40 53 \rangle)/0_3/(0 \mp \langle 47 13 \rangle)]_S$	0.44
$SS_{B,MCA}$	$90/[(0 \mp \langle 59 51 \rangle)/0/(0 \pm \langle 42 15 \rangle)]_S$	$90/[\mp 51/0/\pm 15]_S$	$90/[(0 \mp \langle 41 51 \rangle)/0_3/(0 \pm \langle 46 15 \rangle)]_S$	0.45

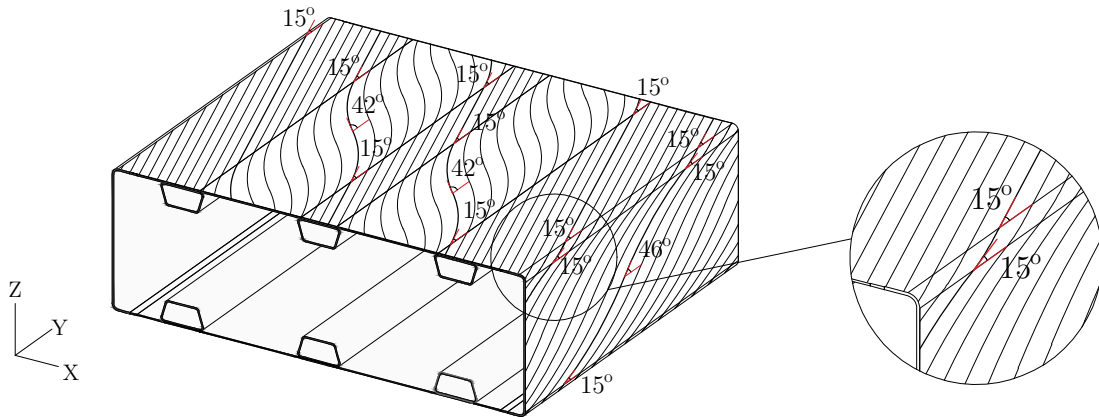


Figure 21: Representation of the 5th layer of  $SS_{B,GA}$ ,  $(0\langle 42|15 \rangle)$  on the skin and  $(0\langle 46|15 \rangle)$  on the spar web. The continuity of the fibre path between the skin and the spar web is highlighted in the magnified detail.

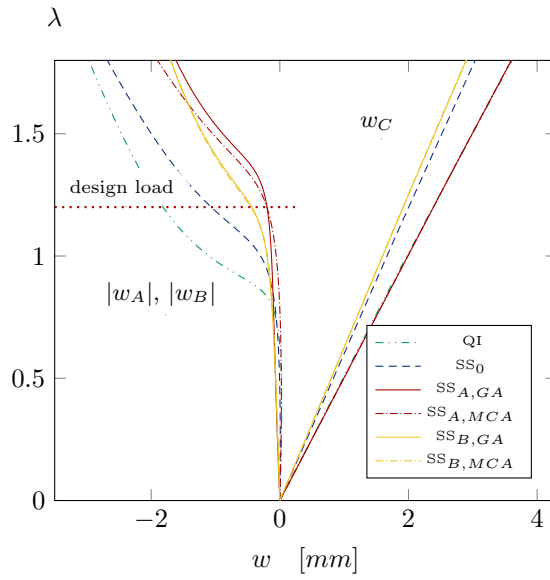


Figure 22: Equilibrium paths of the optimised structures.

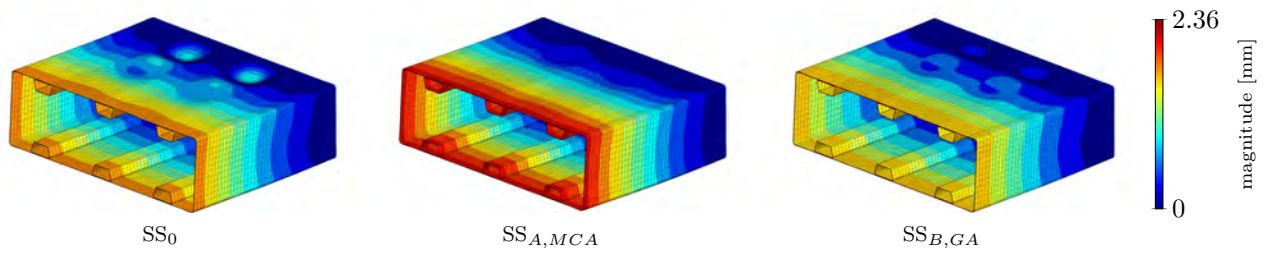


Figure 23: Displacement field at  $\lambda = 1.2$  for the initial and optimised layouts.

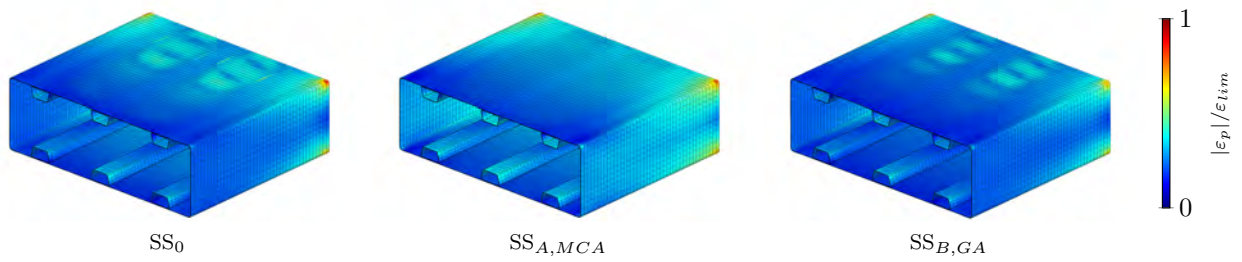


Figure 24: Maximum principal strains normalised for the limit strain of  $2500\mu\epsilon$  at  $\lambda = 1.2$  for the initial and optimised layups.

Figure 23 shows the deformed configurations. It confirms that the solution is the stiffest globally, even if the out-of-plane displacements due to buckling are bigger than in case A. On the other hand, the strains of  $SS_{B,GA}$  are smaller than  $SS_{A,GA}$ , as shown in Fig.24. In particular, the maximum principal strain normalised for the limit strain ( $|\varepsilon_p|/\varepsilon_{lim}$ ) is 0.93 for the initial configuration  $SS_0$ , 0.90 for  $SS_{A,MCA}$  and 0.83 for  $SS_{B,GA}$ .

Table 9: Buckling loads for the stacking sequence  $SS_{C,MCA}$ .

mode	1	2	3	4	5	6	7	8
$\lambda_c$	1.1922	1.1977	1.2420	1.2465	1.2627	1.2705	1.4629	1.4677

Table 10: Stacking sequences and objective function values for case C.

	Skin bay	Skin	Spar web	$w_{c,max}$
$SS_{C,MCA}$	$90/[(0 \pm \langle 57 66 \rangle)/0/(0 \pm \langle 48 26 \rangle)]_S$	$90/[\pm 66/0/\pm 26]_S$	$90/[(0 \pm \langle 63 66 \rangle)/0/(0 \pm \langle 53 26 \rangle)]_S$	0.75
$SS_{C,GA}$	$90/[(0 \mp \langle 56 69 \rangle)/0/(0 \mp \langle 46 24 \rangle)]_S$	$90/[\mp 69/0/\mp 24]_S$	$90/[(0 \mp \langle 53 69 \rangle)/0/(0 \mp \langle 41 24 \rangle)]_S$	0.77

### 5.2.3. Case C

The spar web, having 15 layers, is thicker than the skin (13 layers). We now find an optimised solution considering a uniform thickness, with 13 layers for both skin and spar web. In this way, the weight saving is 6.48%. In fact, the initial skin cross-sectional area is  $4537mm^2$ , the cross-sectional area of the stiffeners is  $2701mm^2$  while the reduced cross-sectional area of the skin is  $4068mm^2$ . The stiffener is again not considered in the optimisation process.

The optimal layup provided by MCA is identified as  $SS_{C,MCA}$ , while that obtained using GA is labelled  $SS_{C,GA}$ . The results obtained are reported in Table 10. In particular, MCA furnishes an improvement of 29% on the out-of-plane displacement and of 4% of on the first buckling load.

Eight buckling modes have been used in the analysis of  $SS_{C,MCA}$ . Their values are reported in Table 9 while Fig.28 shows the first three of them. Figure 25 shows equilibrium paths of the optimised structure and compares it with the previously found optimised solutions. In this case, the importance of a multimodal algorithm is more evident. This is shown by the curves in Fig.26, in which the modal interaction is represented by very similar values assumed by the modal amplitudes of the ROM at the same value of the load. Figure 27 shows the strains and the deformed shape at the design load. It also shows the good agreement between the deformed shapes obtained with Koiter's method and the standard path-following analysis.

### 5.2.4. Comments on the results of the optimisation

In this section we have shown the results of the optimisation process obtained with different scenarios. The best improvement in out-of-plane postbuckling displacement is achieved in case A. However, the maximum tip displacement slightly increases, even if it remains under the design limit. In case B we obtain the globally stiffest solution and, in addition, notable improvements in the buckling and postbuckling performances. Finally, case C highlights the possibility of obtaining a lighter wingbox together with an improved performance in the buckling and postbuckling regime. Table 11 summarises the results obtained for the three analysed cases.

Table 11: Results of the initial and optimised configurations: out-of-plane displacement, first buckling load, maximum tip deflection and area. The improvements are evaluated with respect to  $SS_0$ .

property	initial		optimised			improvements		
	QI	$SS_0$	case A	case B	case C	case A	case B	case C
$w_{C,max}[mm]$	1.82	1.07	0.20	0.44	0.75	81.31%	58.88%	29.91%
$\lambda_{c,1}$	0.93	1.15	1.45	1.31	1.19	25.97%	13.91%	3.48%
$w_{max}[mm]$	2.38	2.00	2.36	1.89	2.38	-17.79%	5.67%	-18.71%
area [ $mm^2$ ]	4537	4537	4537	4537	4068	-	-	6.48%

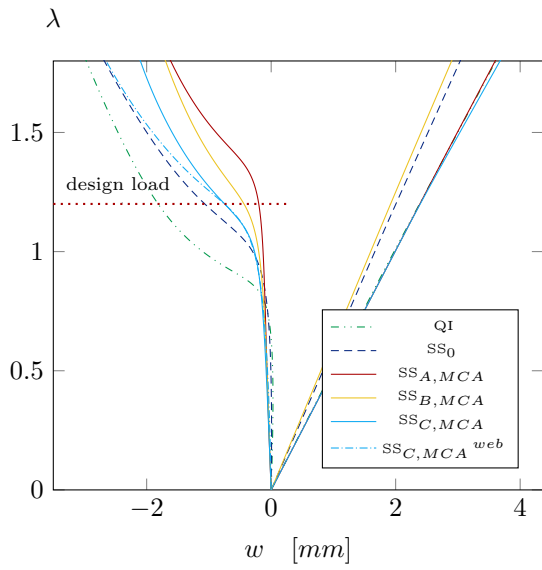


Figure 25: Equilibrium paths of the optimised structures.

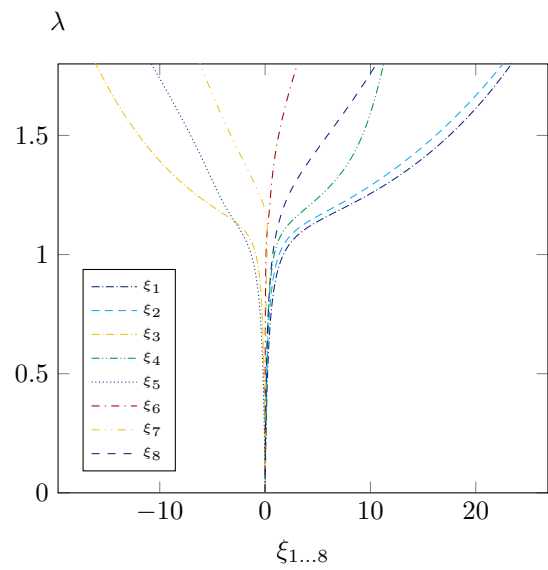


Figure 26: Variables of the ROM for the layup  $SS_{C,MCA}$ .

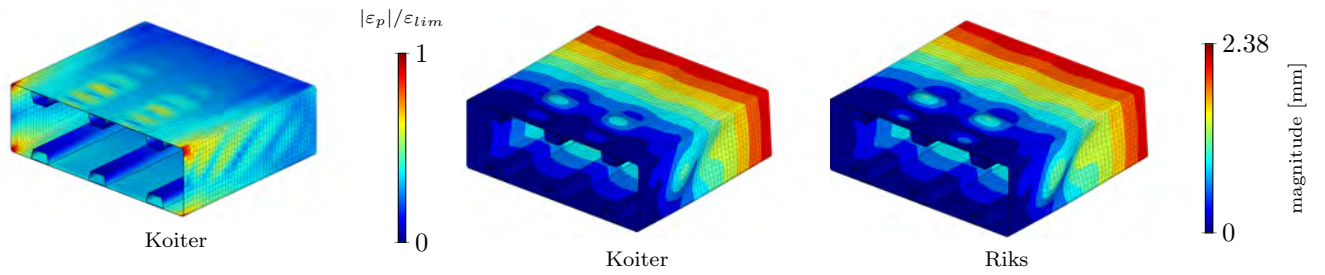


Figure 27: Maximum principal strain normalised with respect to the limit strain on the left and deformed configuration on the right, solution  $SS_{C,MCA}$  and load level  $\lambda = 1.2$ . The wingbox is rotated by  $180^\circ$  with respect to the global  $Z$  to show the buckling on the spar web.

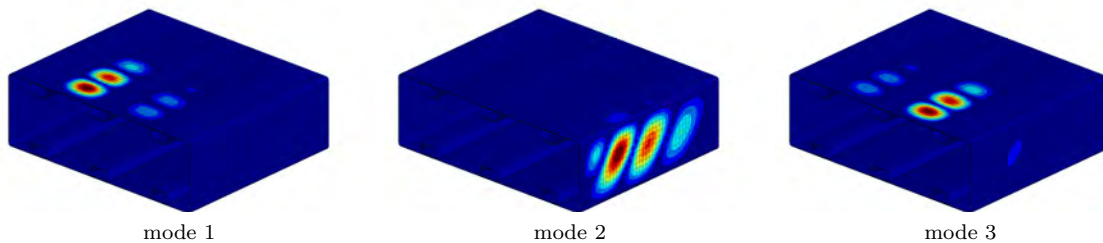


Figure 28: First three buckling modes for the solution  $SS_{C,MCA}$ . The wingbox is rotated by  $180^\circ$  with respect to the global  $Z$  to show the buckling on the spar web.

## 6. Conclusions

In this work an optimisation strategy for the postbuckling behaviour of a VAT wingbox has been proposed. A Koiter-inspired method has been employed to obtain the nonlinear structural response, by coupling it with stochastic algorithms, namely Genetic and Monte Carlo algorithms, for the solution of an optimisation problem. In particular, the FE based multi-modal Koiter approach which takes into account the nonlinear buckling interaction has been used. The reduced order models assembled by this method turns out to be particularly suitable for an optimisation of primary aeronautical structures. The algorithm is based on a first order shear deformation theory hybrid stress solid-shell FE, which in this work has been extended to Variable Angle Tow laminates. It has been shown to be accurate and computationally efficient. Manufacturing constraints, that are essential to obtain a manufacturable laminate, have been included in the optimisation process.

Different optimisation scenarios have been explored. In particular, three optimisation cases have been analysed and improved solutions with respect to the initial baseline structure have been obtained. The first case has given the best solution in terms of buckling and postbuckling behaviour, namely 25.97% in the buckling load and 81.31% reduction in the out-of-plane displacement in the postbuckling regime. In the second case the solution is less improved for the buckling load and out-of-plane postbuckling displacement, however it is globally stiffer than the initial structure. The third case concerns the optimisation of a 6.48% lighter wingbox that still exhibits an improvement of the buckling load of 3.48% and reduction of the out-of-plane displacement in the postbuckling regime of 29.91%. In all cases good agreement has been found between the results obtained with both optimisation algorithms. Finally, for the first case, a study on the influence of the minimum steering radius has been conducted. It shows that small steering radii lead to much better performance in the postbuckling regime. This means that overcoming current manufacturing constraints on the minimum steering radius is worthy of investigation. Future developments of the method will focus on extending the algorithm to design problems expressed in terms of direct stiffness modelling.

## References

- [1] C. Kassapoglou, Design and analysis of composite structures, John Wiley and Sons Ltd.
- [2] V. Oliveri, G. Zucco, D. Peeters, G. J. Clancy, R. Telford, M. Rouhi, C. McHale, R. M. O'Higgins, , T. M. Young, P. M. Weaver, Design, Manufacture and Test of an In-Situ Consolidated Thermoplastic Variable-Stiffness Wingbox, AIAA Journal (2019) 1–13 (2019).
- [3] A. Cooper, Trajectorial fiber reinforcement of composite structures, Department of Mechanical and Aerospace Engineering, Washington University (1972).
- [4] Z. Gürdal, R. Olmedo, In-plane response of laminates with spatially varying fiber orientations - variable stiffness concept, AIAA Journal 31 (4) (1993) 751–758 (1993).
- [5] Z. Gürdal, B. Tatting, C. Wu, Variable stiffness composite panels: Effects of stiffness variation on the in-plane and buckling response, Composites Part A: Applied Science and Manufacturing 39 (5) (2008) 911 – 922 (2008).
- [6] S. Setoodeh, M. M. Abdalla, S. T. IJsselmuiden, Z. Gürdal, Design of variable-stiffness composite panels for maximum buckling load, Composite Structures 87 (1) (2009) 109 – 117 (2009).
- [7] Z. Wu, P. M. Weaver, G. Raju, B. C. Kim, Buckling analysis and optimisation of variable angle tow composite plates, Thin-Walled Structures 60 (Supplement C) (2012) 163 – 172 (2012).
- [8] G. Raju, Z. Wu, B. C. Kim, P. M. Weaver, Prebuckling and buckling analysis of variable angle tow plates with general boundary conditions, Composite Structures 94 (9) (2012) 2961 – 2970 (2012).
- [9] B. H. Coburn, Z. Wu, P. M. Weaver, Buckling analysis of stiffened variable angle tow panels, Composite Structures 111 (Supplement C) (2014) 259 – 270 (2014).
- [10] G. Raju, Z. Wu, P. M. Weaver, Buckling and postbuckling of variable angle tow composite plates under in-plane shear loading, International Journal of Solids and Structures 58 (2015) 270 – 287 (2015).
- [11] S. White, P. Weaver, Towards imperfection insensitive buckling response of shell structures-shells with plate-like post-buckled responses, Aeronautical Journal 120 (1224) (2016) 233–253 (2016).
- [12] R. L. Riche, R. T. Haftka, Optimization of laminate stacking sequence for buckling load maximization by genetic algorithm, AIAA Journal (1993).
- [13] B. H. Coburn, P. M. Weaver, Buckling analysis, design and optimisation of variable-stiffness sandwich panels, International Journal of Solids and Structures 96 (Supplement C) (2016) 217 – 228 (2016).
- [14] E. Barkanov, O. Ozolins, E. Eglitis, F. Almeida, M. C. Bowering, G. Watson, Optimal design of composite lateral wing upper covers. Part I: Linear buckling analysis, Aerospace Science and Technology 38 (Supplement C) (2014) 1 – 8 (2014).
- [15] A. van der Neut, The interaction of local buckling and column failure of thin-walled compression members, in: M. Hetényi, W. G. Vincenti (Eds.), Applied Mechanics, Springer Berlin Heidelberg, Berlin, Heidelberg, 1969, pp. 389–399 (1969).
- [16] W. T. Koiter, M. Pignataro, An alternative approach to the interaction between local and overall buckling in stiffened panels, in: B. Budiansky (Ed.), Buckling of Structures, Springer Berlin Heidelberg, Berlin, Heidelberg, 1976, pp. 133–148 (1976).
- [17] E. Byskov, W. Hutchinson, Mode interaction in axially stiffened cylindrical shells, AIAA Journal 15 (7) (1977) 941–948 (1977).
- [18] K. Rasmussen, G. Hancock, Geometric imperfections in plated structures subject to interaction between buckling modes, Thin-Walled Structures 6 (6) (1988) 433 – 452 (1988).
- [19] E. Barbero, L. Godoy, I. Raftoyiannis, Finite elements for three-mode interaction in buckling analysis, International Journal for Numerical Methods in Engineering 39 (3) (1996) 469–488, cited By 14 (1996).
- [20] V. Gioncu, General theory of coupled instabilities, Thin-Walled Structures 19 (2) (1994) 81 – 127 (1994).
- [21] M. A. Arbelo, R. Degenhardt, S. G. P. Castro, R. Zimmermann, Numerical characterization of imperfection sensitive composite structures, Composite Structures 108 (2014) 295–303 (FEB 2014).
- [22] L. Leonetti, F. Liguori, D. Magisano, G. Garcea, An efficient isogeometric solid-shell formulation for geometrically nonlinear analysis of elastic shells, Computer Methods in Applied Mechanics and Engineering 331 (2018) 159–183 (2018).
- [23] G. Raju, Z. Wu, S. White, P. M. Weaver, Optimal postbuckling design of variable angle tow composite plates, AIAA Journal 56 (2018) 2045 – 2061 (2018).
- [24] E. Riks, An incremental approach to the solution of snapping and buckling problems, International Journal of Solids and Structures 15 (7) (1979) 529–551 (1979).
- [25] M. Crisfield, G. Moita, A unified co-rotational framework for solids, shells and beams, International Journal of Solids and Structures 33 (1996) 2969–2992 (1996).
- [26] Z. Wu, G. Raju, P. M. Weaver, Postbuckling analysis of variable angle tow composite plates, International Journal of Solids and Structures 50 (10) (2013) 1770 – 1780 (2013).
- [27] R. Groh, D. Avitabile, A. Pirrera, Generalised path-following for well-behaved nonlinear structures, Computer Methods in Applied Mechanics and Engineering 331 (2018) 394 – 426 (2018).
- [28] W. Koiter, On the stability of elastic equilibrium, english transl. nasa tt-f10, 883 (1967) and affdl-tr70-25 (1970) Edition, Technische Hooige School at Delft, 1945 (1945).
- [29] S. R. Henrichsen, P. M. Weaver, E. Lindgaard, E. Lund, Post-buckling optimization of composite structures using Koiter's method, International Journal for Numerical Methods in Engineering 108 (8) (2016) 902–940, nme.5239 (2016).
- [30] G. Zagari, G. Zucco, A. Madeo, V. Ungureanu, R. Zinno, D. Dubina, Evaluation of the erosion of critical buckling load of cold-formed steel members in compression based on Koiter asymptotic analysis, Thin-Walled Structures 108 (2016) 193–204 (2016).
- [31] E. Barbero, A. Madeo, G. Zagari, R. Zinno, G. Zucco, Imperfection sensitivity analysis of laminated folded plates, Thin-Walled Structures 90 (2015) 128 – 139 (2015).

- [32] D. Cava, D. Camotim, P. Dinis, A. Madeo, Numerical investigation and direct strength design of cold-formed steel lipped channel columns experiencing local–distortional–global interaction, *Thin-Walled Structures* 105 (2016) 231 – 247 (2016).
- [33] T. Kubiak, M. Urbaniak, G. Zucco, A. Madeo, Imperfection sensitivity analysis of the nonlinear stability of composite beams – numerical and experimental investigations, *Composites Part B: Engineering* 94 (2016) 360 – 369 (2016).
- [34] R. Casciaro, *Computational Asymptotic Post-Buckling Analysis of Slender Elastic Structures*, Phenomenological and Mathematical Modelling of Structural Instabilities - CISM Courses and Lectures NO. 470, SpringerWien, New-York (2005) 195–276 (2005).
- [35] E. Barbero, A. Madeo, G. Zagari, R. Zinno, G. Zucco, Koiter asymptotic analysis of folded laminated composite plates, *Composites Part B: Engineering* 61 (2014) 267–274 (2014).
- [36] T. Rahman, S. T. Ijsselmuiden, M. M. Abdalla, E. L. Jansen, Postbuckling analysis of variable stiffness composite plates using a finite element-based perturbation method, *International Journal of Structural Stability and Dynamics* 11 (04) (2011) 735–753 (2011).
- [37] A. Madeo, R. Groh, G. Zucco, P. Weaver, G. Zagari, R. Zinno, Post-buckling analysis of variable-angle tow composite plates using Koiter’s approach and the finite element method, *Thin-Walled Structures* 110 (2017) 1–13 (2017).
- [38] D. Magisano, L. Leonetti, G. Garcea, Advantages of the mixed format in geometrically nonlinear analysis of beams and shells using solid finite elements, *International Journal for Numerical Methods in Engineering* 109 (9) (2017) 1237–1262 (2017).
- [39] D. Magisano, K. Liang, G. Garcea, L. Leonetti, M. Ruess, An efficient mixed variational reduced-order model formulation for nonlinear analyses of elastic shells, *International Journal for Numerical Methods in Engineering* 113 (4) (2018) 634–655 (2018).
- [40] L. Leonetti, D. Magisano, F. Liguori, G. Garcea, An isogeometric formulation of the Koiter’s theory for buckling and initial post-buckling analysis of composite shells, *Computer Methods in Applied Mechanics and Engineering* 337 (2018) 387 – 410 (2018).
- [41] B. G. Falzon, M. H. Aliabadi, *Buckling and postbuckling structures: Experimental, analytical and numerical studies*, Imperial College, London, U.K. (2008) 177–224 (2008).
- [42] F. S. Liguori, A. Madeo, D. Magisano, L. Leonetti, G. Garcea, Post-buckling optimisation strategy of imperfection sensitive composite shells using Koiter method and Monte Carlo simulation, *Composite Structures* 192 (2018) 654 – 670 (2018).
- [43] T. M. Young, *Performance of the jet transport airplane: analysis methods, flight operations and regulations*, Wiley, December 2017 (December 2017).
- [44] G. Clancy, D. Peeters, Vincenzo, D. Jones, R. M. O’Higgins, P. M. Weaver, A study of the influence of processing parameters on steering of carbon fibre/peek tapes using laser-assisted tape placement, *Composites Part B: Engineering* (2018).
- [45] K. Ikeda, K. Murota, Asymptotic and probabilistic approach to buckling of structures and materials, *Applied Mechanics Reviews* 61 (2008) 040801 – 040801–16 (2008).
- [46] M. Deml, W. Wunderlich, Direct evaluation of the ‘worst’ imperfection shape in shell buckling, *Computer Methods in Applied Mechanics and Engineering* 149 (1) (1997) 201 – 222, containing papers presented at the Symposium on Advances in Computational Mechanics (1997).
- [47] K. Sze, W. Chan, T. Pian, An eight-node hybrid-stress solid-shell element for geometric non-linear analysis of elastic shells, *International Journal for Numerical Methods in Engineering* 55 (7) (2002) 853–878 (2002).
- [48] D. Magisano, L. Leonetti, G. Garcea, Koiter asymptotic analysis of multilayered composite structures using mixed solid-shell finite elements, *Composite Structures* 154 (2016) 296–308 (2016).
- [49] G. Zucco, R. Groh, A. Madeo, P. Weaver, Mixed shell element for static and buckling analysis of variable angle tow composite plates, *Composite Structures* 152 (Supplement C) (2016) 324 – 338 (2016).
- [50] T. Macquart, A. Pirrera, P. M. Weaver, Finite beam elements for variable stiffness structures, *AIAA Journal* 56 (2018) 3362 – 3368 (2018).
- [51] G. Garcea, F. S. Liguori, L. Leonetti, D. Magisano, A. Madeo, Accurate and efficient a posteriori account of geometrical imperfections in Koiter finite element analysis, *International Journal for Numerical Methods in Engineering* 112 (9) (2017) 1154–1174, nme.5550 (2017).
- [52] Z. Wu, G. Raju, P. M. Weaver, Framework for the buckling optimization of variable-angle tow composite plates, *AIAA Journal* 53 (2015) 3788 – 3804 (2015).
- [53] O. Stodieck, J. E. Cooper, P. M. Weaver, P. Kealy, Aeroelastic tailoring of a representative wing box using tow-steered composites, *AIAA Journal* 55 (2016) 1425 – 1439 (2016).
- [54] M. A. Albazzan, R. Harik, B. F. Tatting, Z. Gürdal, Efficient design optimization of nonconventional laminated composites using lamination parameters: A state of the art, *Composite Structures* 209 (2019) 362 – 374 (2019).
- [55] K. Deep, K. P. Singh, M. Kansal, C. Mohan, A real coded genetic algorithm for solving integer and mixed integer optimization problems, *Applied Mathematics and Computation* 212 (2) (2009) 505 – 518 (2009).
- [56] K. Deb, An efficient constraint handling method for genetic algorithms, *Computer Methods in Applied Mechanics and Engineering* 186 (2) (2000) 311 – 338 (2000).
- [57] G. Zucco, V. Oliveri, D. Peeters, R. Telford, G. J. Clancy, C. McHale, M. Rouhi, R. M. O’Higgins, P. M. Weaver, Static test of a thermoplastic compositewingbox under shear and bending moment, 2018 AIAA/ASCE/AHS/ASC Structures, Structural Dynamics, and Materials Conference (2018).